

Computational Mechanics  
Research and Support  
for Aerodynamics and Hydraulics  
at **TFHRC**



Quarterly Report

September through December 2010

**Y1Q1**



**Computational Mechanics Research and Support  
for Aerodynamics and Hydraulics at TFHRC  
Year 1 Quarter 1 Progress Report**

**Energy Systems Division (ES)  
Argonne National Laboratory (ANL)**

**Principal Investigators:  
Steven A. Lottes, Ph.D.**

**Ronald F Kulak, Ph.D., PE, FASME**

**Contributor:  
Cezary Bojanowski, Ph.D.**

**Submitted to:  
Federal Highway Administration**

**Kornel Kerenyi, Ph.D.  
Turner-Fairbank Highway Research Center  
Federal Highway Administration  
6300 Georgetown Pike  
McLean, VA 22101**

**Harold Bosch, Ph.D.  
Turner-Fairbank Highway Research Center  
Federal Highway Administration  
6300 Georgetown Pike  
McLean, VA 22101**

**January, 2011**

## Table of Contents

1	Introduction and Objectives.....	7
2	Computational Fluid Dynamics Technical Section .....	8
2.1	First-Year CFD Tasks .....	8
2.1.1	Test Mesh Morphing Applied to Clear Water Pressure Flow Scour.....	8
2.1.2	Run RANS Simulations for Rectangular Bridge Pier Project .....	11
2.1.3	Review Entrainment Functions for RANS Scour Models and Plan Tests of Alternatives ....	11
2.1.4	Develop 3D Culvert Flow Simulation Procedure to Obtain Losses .....	14
2.1.5	Test CFD Analysis of Wind Loads on Single Bridge Decks .....	18
3	Computational Multiphysics Mechanics Technical Section .....	20
3.1	Technical Background .....	20
3.2	Technical Approach.....	21
3.3	First-Year Tasks .....	22
3.3.1	Hybrid Multiphysics Analysis of Stay Cables .....	22
3.3.2	Multiphysics Analysis of Stay Cables.....	22
3.3.3	Traffic and Wind Loading of Stay Cable Bridges .....	23
3.3.4	Stability of Bridges with Piers in Scour Holes.....	39
3.3.5	Modeling of Salt-Spray Transport Beneath Steel Bridges .....	64

## List of Figures

Figure 2.1: Maximum bed shear stress plotted to 40 hours of simulated time, with remeshing at 36 and 360 seconds .....	9
Figure 2.2: Maximum bed recession rate plotted to 40 hours with remeshing at 36 and 360 seconds ....	10
Figure 2.3: Velocity field and scour hole contour at 40 hours for simplified test case .....	10
Figure 2.4: Scour rates for various velocities with no bridge blockage in the TFHRC scour flume with 2 mm sand .....	14
Figure 2.5: Diagram of the experimental culvert flow flume at the Turner-Fairbank Highway Research Center .....	15
Figure 2.6: Experimental culvert flow flume at TFHRC with view from upstream end .....	15
Figure 2.7: Computational domain for laboratory scale culvert flow CFD computation .....	16
Figure 2.8: Streamlines through culvert flume showing separation of flow in the exit section of the culvert with a large recirculation zone .....	18
Figure 2.9: Water height and velocity distributions in culvert cross sections showing effects of the asymmetric exit geometry upstream halfway between the culvert barrel entry and exit .....	18
Figure 3.3.1: Dynamic model of stay cable .....	25
Figure 3.3.2: Comparison of Finite Element solution to analytical solution for cable parametric vibrations: (a) in line with exciting force – analytical (b) in line with exciting force – Finite Element .....	26
Figure 3.3.3: Bill Emerson Memorial Bridge .....	27
Figure 3.3.4: FE model of Bill Emerson Memorial Bridge – view of the deck structure .....	29
Figure 3.3.5: FE model of Bill Emerson Memorial Bridge with numbering of the stay cables .....	30
Figure 3.3.6: First seven global mode shapes for FE model of the Bill Emerson Memorial Bridge .....	32
Figure 3.3.7: Northridge earthquake (a) vertical acceleration history (b) Fourier Transform of the history .....	33
Figure 3.3.8: Response of the bridge model to the Northridge earthquake (a) Deflection history at the mid-span (b) Lateral vibrations of tower and cable 32 .....	34
Figure 3.3.9: Simplified FE model of the AASHTO HS 20-44 truck .....	35

Figure 3.3.10: Response of the bridge to the traffic loading (a) Deflection history at the mid-span (b) Lateral vibrations of cable 32.....	36
Figure 3.3.11: Oat Ditch Bridge on I-15 in California (a) failed column (b) column footing .....	40
Figure 3.3.12: Triaxial hydrostatic compression data for soil material (3) .....	42
Figure 3.3.13: Numerical model for the soil penetration test simulation .....	42
Figure 3.3.14: Deformations and vertical stresses at 15 inches of penetration: (a) Lagrange (b) EFG (c) SPH (d) MM-ALE .....	43
Figure 3.3.15: Simulation results for force as a function of loading pad penetration: Lagrange, EFG, SPH and MM-ALE (a) original results (b) comparison to experiment .....	44
Figure 3.3.16: Effect of loading rate on force vs. penetration results: (a) Lagrangian (b) EFG (c) SPH (d) MM-ALE.....	45
Figure 3.3.17: Effect of mesh size on force vs. penetration results (a) Lagrangian (b) EFG (c) SPH (d) MM-ALE.....	46
Figure 3.3.18: Numerical model for the cone penetration test simulation: (a) Hybrid Lagrangian-SPH model (b) MM-ALE model.....	49
Figure 3.3.19: Triaxial hydrostatic compression data for soil materials .....	49
Figure 3.3.20: CPT data for Norfolk Sand.....	50
Figure 3.3.21: CPT data for Decatur Clay .....	52
Figure 3.3.22: Deformations and vertical stresses at 210 mm of penetration: (a) SPH (b) MM-ALE .....	52
Figure 3.3.23: Energy Balance for CPT test simulation .....	53
Figure 3.3.24: CPT simulations results for different friction coefficients between cone and soil .....	53
Figure 3.3.25: Elliptic paraboloid for representing the surface of a scour-hole: top view on left; perspective view on right.....	57
Figure 3.3.26: Oat Ditch Bridge on I-15 in California (a) failed column (b) column footing .....	58
Figure 3.3.27: Computational model of the bent cap, column and soil of the Oat Ditch Bridge .....	59
Figure 3.3.28: Displacement of the footing as a function of time .....	61
Figure 3.3.29: Deformation in the soil and the column for Case 3.....	61
Figure 3.3.30: Bridge pier with footing embedded in a scour-hole represented by a regularized elliptic paraboloid .....	62

Figure 3.3.31: Displacement of the footing as a function of time .....	63
Figure 3.3.32: Semitrailer traveling through a bridge underpass.....	64
Figure 3.3.33: Mack CH 613 tractor (a) schematics (b) FE model of the tractor with a sleeper .....	65
Figure 3.3.34: FE model of the tractor with trailer .....	65
Figure 3.3.35: Semitrailer truck entering a bridge underpass .....	66
Figure 3.3.36: Semi-trailer truck impacting a layer of air in a bridge underpass: (a) at the beginning of the simulation; and (b) at simulation time of 0.40 seconds .....	67
Figure 3.3.37: Finite Element model of a Tire traveling through thin layer of water (a) Model of a tire traveling through a thin layer of water (b) computational mesh for air domain .....	68
Figure 3.3.38: Finite Element model of a Tire traveling through thin layer of water.....	69

## List of Tables

Table 2.1 Comparison of flume tilt needed to balance flow losses for three tested CFD analysis methods and the value obtained using Manning’s formula for fully developed flow .....	17
Table 3.1: Model properties.....	25
Table 3.2: Averaged properties of the cables in FE model of Bill Emerson Memorial Bridge (6) .....	30
Table 3.3: Comparison of natural frequencies of the FE model with experimental values.....	33
Table 3.4: Vehicle model stiffness and mass properties (10) .....	36
Table 3.5: Parameters used to define soil material using formulation MAT_005 (units: mm-s-tonne).....	41
Table 3.6: Simulation statistics at a penetration depth of 5 inches.....	46
Table 3.7: Parameters used to define soil materials using formulation MAT_005 (SI units: mm-second-tonne).....	49
Table 3.8: Computational statistics.....	67



# 1 Introduction and Objectives

This project was established with a new interagency agreement between the Department of Energy and the Department of Transportation to provide collaborative research, development, and benchmarking of advanced three-dimensional computational mechanics analysis methods to the aerodynamics and hydraulics laboratories at the Turner-Fairbank Highway Research Center for a period of five years, beginning in October 2010. The analysis methods employ well-benchmarked and supported commercial computational mechanics software and also include user subroutines, functions, and external software programs and scripts written to automate the analysis procedures. Computational mechanics encompasses the areas of Computational Fluid Dynamics (CFD), Computational Wind Engineering (CWE), Computational Structural Mechanics (CSM), and Computational Multiphysics Mechanics (CMM) applied in Fluid-Structure Interaction (FSI) problems.

The major areas of focus of the project are wind and water loads on bridges — superstructure, deck, cables, and substructure (including soil), primarily during storms and flood events — and the risks that these loads pose to structural failure. For flood events at bridges, another major focus of the work is assessment of the risk to bridges caused by scour of stream and riverbed material away from the foundations of a bridge. The work plan encompasses tasks that start the development and benchmarking of models with simple physics models that will run economically and quickly on current computer hardware. The benchmarking against experimental data will determine the range of applications and conditions in which these simple models can be applied with adequate accuracy and good engineering safety margins. Models that are judged sufficient and useful for application can then be applied in field applications. Tasks in succeeding years are defined to include more complex physics in the models and, in some cases, account for interactions between different types of physics occurring in the fluid and solid materials in fluid-structure interaction problems. As time passes, the commercial computational mechanics software is expected to improve substantially, incorporating additional physics models and capabilities. The project tasks will take advantage of the relevant improvements as they become available and can be tested. Computer hardware capabilities are also expected to increase, enabling the solution of problems with more complex physics increasingly practical.

This quarterly report documents technical progress on the project tasks for the period of October through December 2010.

## 2 Computational Fluid Dynamics Technical Section

### 2.1 First-Year CFD Tasks

#### 2.1.1 Test Mesh Morphing Applied to Clear Water Pressure Flow Scour

Mesh morphing is a method for moving the computational mesh, primarily in fluid structure interaction (FSI) problems, in the STAR-CCM+ CFD software. In the mesh morphing process, the mesh is moved in a way that is designed to maintain a high mesh quality and accurate simulation results as the mesh moves in response to boundary or interface motion. In FSI problems boundary deformation is normally computed in computation structural mechanics software and occurs primarily in response to normal forces. In scour problems, bed motion is erosion or sediment settling deposition, and the erosion is driven by unsteady interactions with turbulent eddies. The erosion is usually correlated with riverbed shear stresses. While the driving forces for boundary motion in FSI problems and scour are different, the need to maintain a high quality mesh as the mesh is moved to follow the motion of the boundary is shared between these problems. Therefore, the use of mesh morphing is a way to leverage the software development effort by CD-adapco for FSI problems to solve scour modeling problems. A more detailed discussion of some of the problems encountered in the application of mesh morphing to scour problems along with figures can be found in the TRACC Quarterly Report for Year 5 Quarter 1, H. Ley, January 2011. The technique was tested on a thin nearly two-dimensional slice through a pressure flow scour flume to verify that it would work with periodic remeshing. After several rounds of problem resolution, the techniques were found to work well on the test problem with the computation carried out to several days of simulated time needed for some pressure flow scour experiments to approach equilibrium scour conditions.

The computation procedure is as follows. The simulation is run for 1 to 2 residence times with no scouring (bed and volume mesh morphing) by setting the bed velocity to zero using a field function, "initialbedvel," defined as [0,0,0]. A residence time is about 12 seconds. Starting from an initial flow field set to the inlet velocity of 0.53 m/s, the shear stress on the bed will not be physically realistic. After

between 1 and 2 residence times, 12 to 24 seconds, the initial non-realistic conditions will die out as the boundary layer over the bed has a chance to develop. A start up time of 12 seconds was used for the initial tests.

For the purposes of computing scour using a k-epsilon turbulence model and wall functions to determine the shear stress at the wall, the bed roughness is taken to be  $2 \cdot d_{50} = 4$  mm for 2 mm sand. According to the STAR-CCM+ manual, the wall functions require that the roughness height be equal to or less than the cell centroid of the near wall cell. Therefore the near wall cells should be 8 mm high to satisfy this requirement. This height yields a *yplus* value for near wall cells between 110 and 200, except near the inlet where it is about 230 and the shear stress also spikes up because of the uniform inlet condition. Those values are a little high but probably provide reasonable accuracy. Further testing compared to experiment is planned, and the adequacy of the model can be assessed based on those results.

At the beginning of the simulation the scour rate is rapid and on the order of a fraction of a millimeter per second. As the scour process removes bed material, the maximum local bed shear stress drops rapidly as shown in Figure 2.1 and the scour rate drops rapidly as well as shown in Figure 2.2.

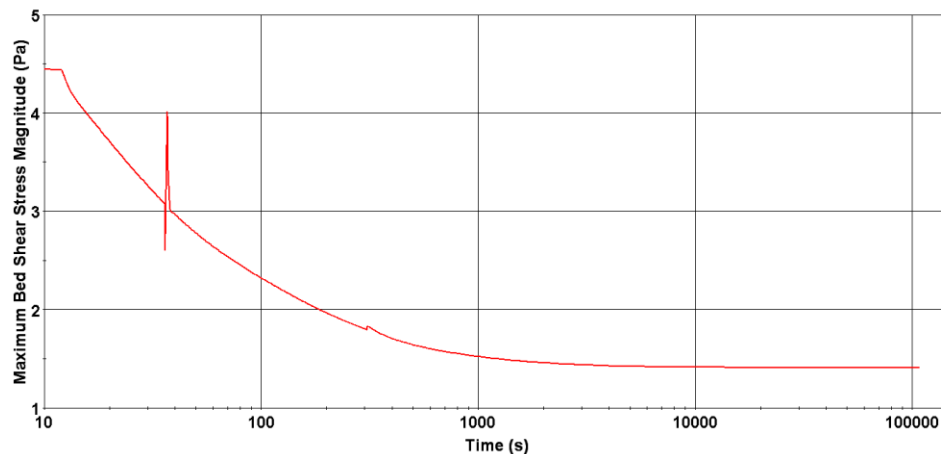


**Figure 2.1: Maximum bed shear stress plotted to 40 hours of simulated time, with remeshing at 36 and 360 seconds**

A major hurdle in modeling scour events that occur over hours or days is the huge difference in flow and scour time scales. The flow time scale depends on the cell size in the computational mesh and is typically on the order of milliseconds, while the erosion time scale may vary from a fraction of a second up to hours. Attempting to use CFD software to compute a scour event at the flow time scale may, in most cases take weeks to many months of computer and real time, even on large parallel cluster computers because the time dimension cannot be parallelized. To bridge these time scales and reduce the problem to one that can be solved in a day or two, Reynolds Averaged Navier-Stokes equations are used to solve for the flow field and shear stresses on the flume or river bed with a semi-implicit solver using a turbulence model like the k-epsilon model. When scour is not changing the bed topology

rapidly, the flow field reaches a quasi-steady state with these models, and the time step can be set to maintain the quasi-steady conditions by setting it to a value that yields a maximum bed displacement that is a fraction of the near bed computational cell height. At the start of the computation from initial flat bed conditions, when the scour rate is near a millimeter per second, the time step will be a small fraction of a second. As the scour approaches equilibrium or asymptotic conditions, the flow field becomes nearly steady in the mean, and the time step can be increased up to minutes and even hours. The test case was run out to 40 hours of simulated time, and as shown in Figure 2.2, the bed recession rate due to scour at that time is down to a fraction of a nano-meter per second. In comparison, the scour rate in the channel of the Grand Canyon is on the order of three pico-meters per second.

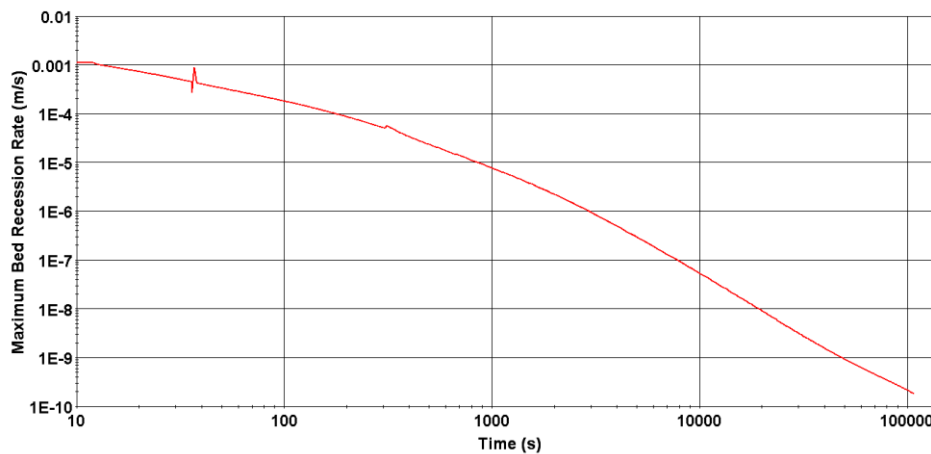


**Figure 2.2: Maximum bed recession rate plotted to 40 hours with remeshing at 36 and 360 seconds**

The velocity field with the final scour hole profile is shown in Figure 2.3 for the simplified test case that was run. The scour hole contour is smooth and qualitatively similar to those obtained using STAR-CD and a much more complicated cyclic running procedure that did not use mesh morphing and required remeshing after each iteration of bed displacement.

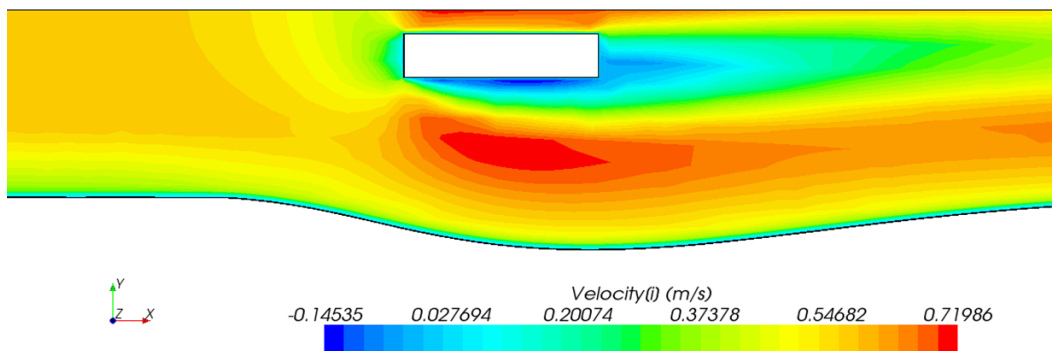


**Figure 2.3: Velocity field and scour hole contour at 40 hours for simplified test case**

This methodology appears to provide a good foundation for a transient scour model. The sediment entrainment rate used for the test case was a correlation of Van Rijn (1). The maximum scour depth and

the rate of formation of the scour hole are sensitive to the entrainment rate function. Initial efforts to identify suitable forms of entrainment rate functions are discussed below.

### 2.1.2 Run RANS Simulations for Rectangular Bridge Pier Project

A student from Northern Illinois University will be working on scour analysis methods applied to rectangular bridge piers using Reynolds Averages Navier-Stokes turbulence models. This effort is still in the early stages with the student learning how to use the STAR-CCM+ software and running some sample cases from a student who graduated who was working on cylindrical bridge piers.

### 2.1.3 Review Entrainment Functions for RANS Scour Models and Plan Tests of Alternatives

Transient modeling of scour requires an entrainment rate function to compute the rate of material removal from the sediment bed. When the model includes sediment transport, the sediment transport equation or equations, if a size spectrum of particles is modeled, will have source and sink terms for sediment entrainment and sediment settling back onto the bed. Some approaches use correlations to determine the bed load and then obtain the entrainment rate by doing a mass balance on computational cells that span the thin bed load layer. In this case, the net outflow of particles from a cell is taken as the entrainment rate. This value can be negative and is the net rate of accumulation of sediment on the bed due to a sediment settling rate that exceeds the entrainment rate. For clear water scour, or a conservative estimate of scour, the settling of sediment can be ignored, and the entrainment rate will correspond to a bed recession rate due to scour.

Several forms of entrainment rate or pick up rate functions can be used. The fundamental physics of entrainment is not currently sufficiently understood to provide a formulation based on the fundamental physics, and even if such a formulation were available, it would be operating at length and time scales that would require too many computational resources and computer time to compute realistic scour by floods.

A common engineering practice is to determine via experiment and data correlation a critical shear stress needed to set sediment particles into motion. The sediment entrainment rate, which is also a component of the bed recession rate due to scour, can then be formulated as a function of the difference between the bed shear stress and the critical bed shear stress. The Van Rijn entrainment function used in the test is based on this type of formulation.

It is a power law function that has the form:

$$E_b = A_0 \left( \frac{\tau}{\tau_c} - 1 \right)^n \text{ for } \tau > \tau_c \quad (2.1)$$

$$E_b = 0 \text{ for } \tau < \tau_c \quad (2.2)$$

where  $A_0$  and  $n$  are fitting parameters, and  $E_b$  is the sediment pickup rate in units of mass per unit sediment bed area and per unit time,  $\text{kg}/(\text{m}^2 \text{ s})$ . In the absence of material settling back on the bed, the bed recession rate due to entrainment only is:

$$\frac{\partial h}{\partial t} = \frac{1}{\varepsilon_0} \frac{E_b}{\rho_s} \quad (2.3)$$

where,  $h$  is the height of the sediment bed,  $\varepsilon_0$  is the sediment packing density and  $\varepsilon_0 = (1 - \lambda_0)$  where  $\lambda_0$  is the bed porosity, and  $\rho_s$  is the sediment density. Using Van Rijn's correlation for the pickup rate gives:

$$\frac{\partial h}{\partial t} = -b_0 \left[ \frac{\tau_b}{\tau_c} - 1 \right]^{1.5} \quad (2.4)$$

where

$$b_0 = \frac{a_0 d_*^{0.3} \sqrt{(s-1)g d_{50}}}{\varepsilon_0} \quad (2.5)$$

and

$$d_* = \left[ \frac{(s-1)g}{\nu^2} \right]^{1/3} d_{50} \quad (2.6)$$

where  $s = \rho_s/\rho$  is the ratio of sediment,  $\rho_s$ , to water density,  $\rho$ ,  $\nu$  is the kinematic viscosity,  $d_{50}$  is the mean diameter of sediment,  $g$  is the acceleration due to gravity,  $\tau_c$  is the critical shear stress,  $d_*$  is a dimensionless sediment diameter, and  $a_0 = 0.00033$  is a constant that Van Rijn obtained by correlating data for different particle sizes ranging from 130  $\mu\text{m}$  to 1.5 mm. For  $d_{50} = 2$  mm sand the critical shear stress is 1.41 Pa and  $b_0 = 0.00035$ . These values were used in the initial testing of the method described in the mesh morphing section.

As noted in the previous section on the mesh morphing, the goal of the initial work with this method was to establish the procedure and ensure that it functioned on a very simple case. With the procedure established, the options for sediment entrainment functions are being evaluated for testing against the TFHRC transient pressure flow scour experiments. The power law entrainment function of Van Rijn is one option. One of the limitations of formulation given in Equation 2.2 is that the scour rate is zero when the mean bed shear stress is less than or equal to the critical shear stress. In reality, turbulent fluctuations when the mean shear stress is less than but near the critical value do cause motion of particles in the bed and causes the formation of bed forms far upstream of a flood deck blockage in laboratory experiments. A Naval Research Laboratory report (2) on pick up functions for cohesive soils discusses the difficulties in determining rate laws that can be used outside the range of the conditions of the experimental data including particle size. A variety of functions can be fitted within the often

narrow ranges of available data. The report suggests that an exponential law may better characterize entrainment and proposes a function of the form:

$$E_b = \epsilon_0 \exp \left[ \frac{\tau}{\alpha} \right] \quad (2.7)$$

This type of function may have a curvature that represents the dependence on shear stress over some of the range of the independent variable, however, it has the problem that the entrainment rate does not approach zero as the shear stress approaches zero. A literature review of entrainment rate functions is being conducted. Published work in this area appears to be sparse due to the difficulty of running experiments to determine both the entrainment rate and bed shear stress.

An entrainment function form that is analogous to a chemical kinetic rate law is proposed by Lottes (3) and has the form:

$$E_b = A_0 \left( \frac{\tau}{\tau_c} \right)^n \exp \left( -\frac{A_1 \tau_c}{\tau} \right) \quad (2.8)$$

where  $A_0$ ,  $A_1$ , and  $n$  are fitting parameters.

This form of entrainment function has exponential decay as the bed shear stress approaches zero. It also has the correct value of zero entrainment rate when the bed shear stress is zero. The  $(\tau / \tau_c)^n$  term determines the behavior of  $E_b$  when the bed shear,  $\tau$ , is large, since the exponential term approaches 1 for large  $\tau$ . The critical shear stress,  $\tau_c$ , is no longer a value of bed shear stress where the entrainment rate becomes zero, rather it is a value of shear stress beyond which the entrainment rate grows rapidly. This form allows for a smooth transition between the condition of high, low, and insignificant scour rates, where the meaning of these terms depends on the length of the flood or the time scale of interest. It has the capability to represent the relatively slow scour rate of rock over years, decades, or even geologic time scales. Note that scour rates for rock are of interest for some types of rock that can undergo significant scour in the time span of the service life of a bridge.

In addition to data from the literature and reported fitting constants for entrainment functions, TFHRC has data from a set of experiments run in 2009 with 2 mm mean diameter sand to check the critical velocity in the flume being used for pressure flow scour experiments. The experiments give the sediment removal rate over the test section as a function of the velocity with no bridge deck in the flume. The data from these experiments can be used to determine an entrainment rate function for 2 mm sand. Because the experiments give entrainment rate or bed recession rate as a function of the mean flow velocity, the bed shear stress that corresponds to each of the velocities needs to be determined. The Colebrook-White correlation and some variations of it give the bed shear in terms of the mean flow velocity, with assumptions such as fully developed flow and a pipe or channel with constant roughness. In the laboratory test flume, neither of these conditions is met. One of these is the fully developed flow, which is not the case in the pressure flow scour experiments, since the entry

length is only about 4 m. In addition, the flume bed has a  $4 \text{ mm} = 2 d_{50}$  effective roughness for 2 mm sand, but the flume walls, which make up a large portion of the hydraulic diameter, are smooth.

A good way to determine the bed shear stress that corresponds to each of the experimental flow velocities and measured scour rates is to use the STAR-CCM+ CFD code to determine the mean bed shear over the section of the flume corresponding to the test section. This work is currently being carried out. The mean velocity versus scour rate data from these experiments is shown in Figure 2.4. Once the mean shear stress corresponding to the velocities of the experiments is determined, the data relating shear stress with entrainment rate can be used to fit parameters for any of the sediment pickup function forms. The fitted pickup functions will then be used in transient pressure flow scour CFD simulations and checked against experiment.

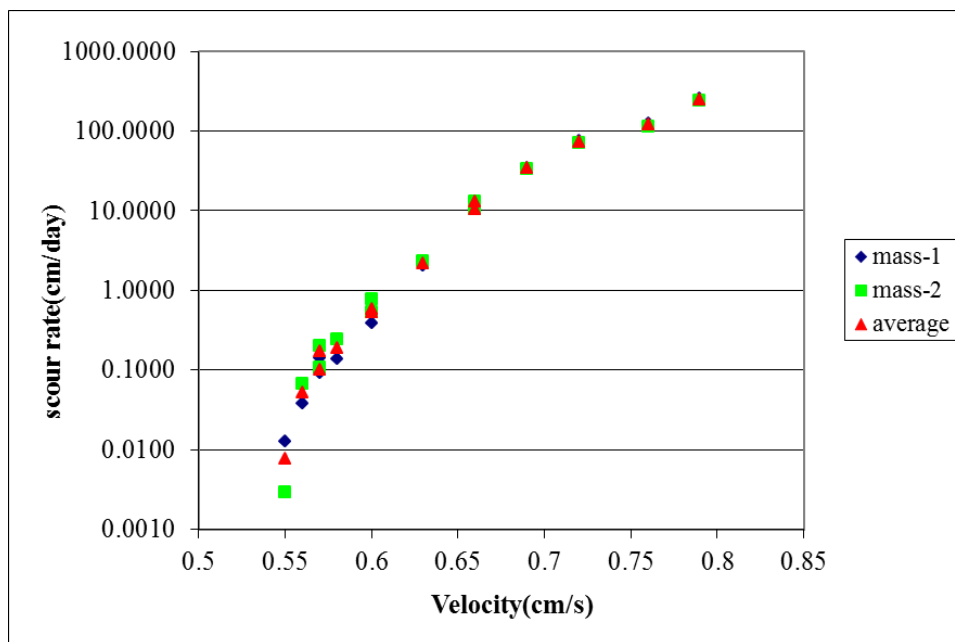


Figure 2.4: Scour rates for various velocities with no bridge blockage in the TFHRC scour flume with 2 mm sand

### 2.1.4 Develop 3D Culvert Flow Simulation Procedure to Obtain Losses

An initial effort to investigate methods for using CFD to determine a loss coefficient for culverts with varying barrel design geometry was completed. Three approaches to computing the head loss in a culvert barrel for given flow conditions were investigated and compared to experiment. This work was carried out over the past year and reported in quarterly reports. A summary of the methods, comparisons with experiment, conclusions, and recommendations for follow on work are presented here.

The CFD culvert flow computations were compared to culvert flow experiments conducted at TFHRC. A diagram of the full culvert experimental flume at TFHRC is shown in Figure 2.5, and a picture of the flume in operation is shown in Figure 2.6.



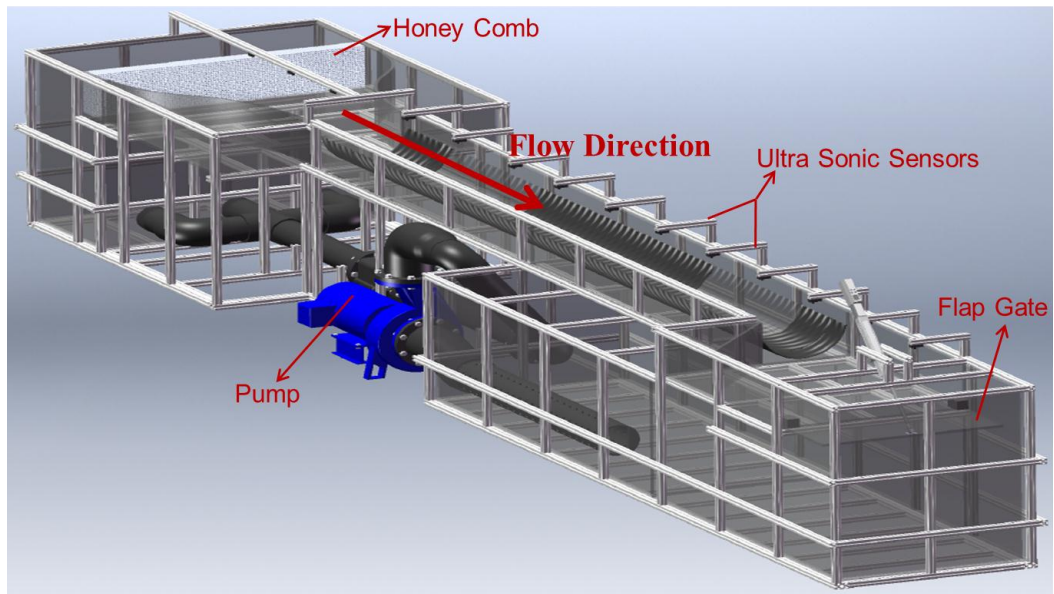


Figure 2.5: Diagram of the experimental culvert flow flume at the Turner-Fairbank Highway Research Center

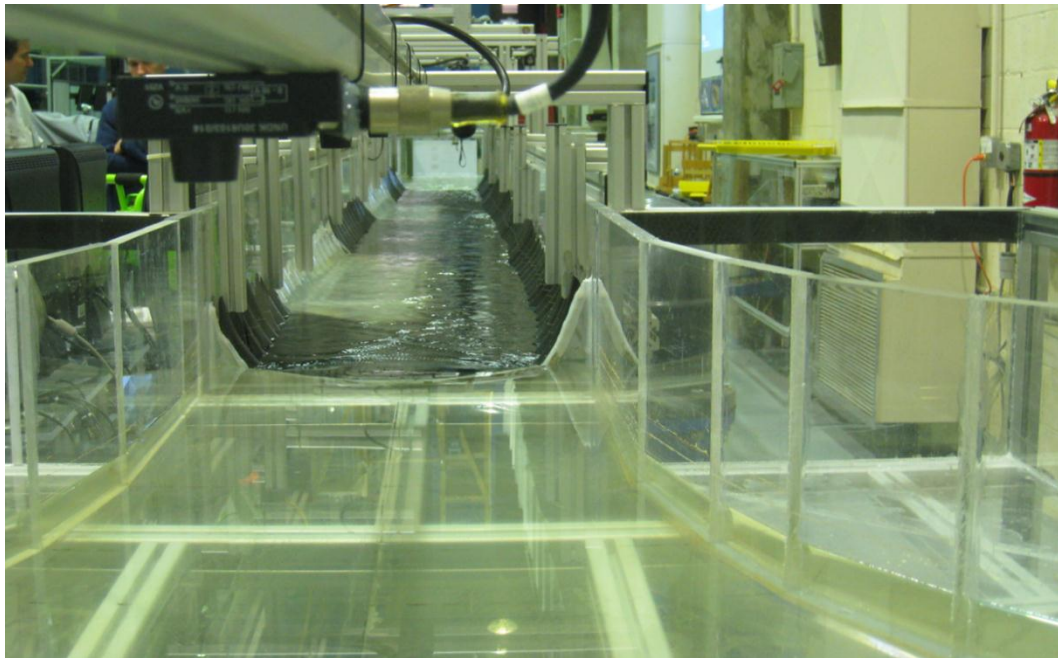
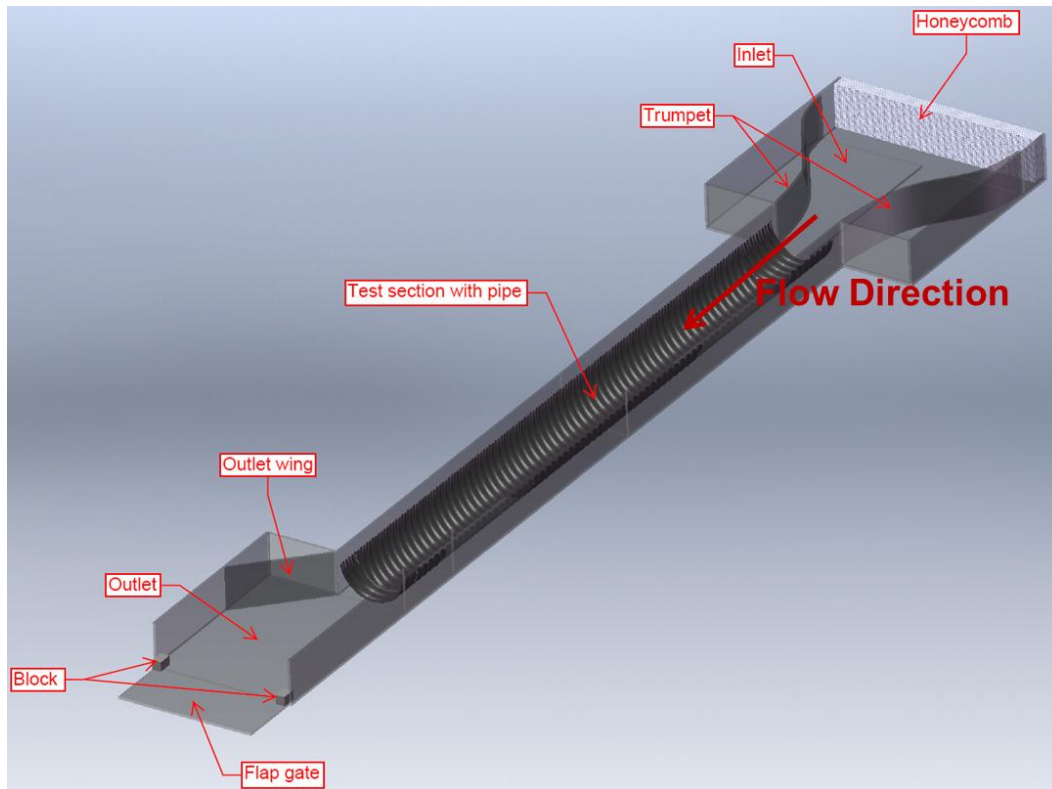


Figure 2.6: Experimental culvert flow flume at TFHRC with view from upstream end.

Only the geometry from the honeycomb inlet to the drop off at the end of the flap gate is needed for CFD computations, however, and this portion of the flume flow geometry is represented very accurately in the CFD computations to ensure that all of the effects in the flow that are a consequence of the geometry are accounted for in the CFD model. For example there was a symmetric trumpet reducing

the flow area at the barrel inlet, but an asymmetric diffuser at the barrel outlet. The portions of the geometry used in the CFD model are shown in Figure 2.7.



**Figure 2.7: Computational domain for laboratory scale culvert flow CFD computation**

Three methods for computing head loss in the barrel were investigated. The losses are primarily a consequence of turbulence dissipation from vortex structures generated by flow over the corrugations of the barrel. The methods are:

1. Use iterative CFD computations to determine a tilt angle that yields a constant water depth for the flow through the culvert barrel.
2. Compute the difference between the kinetic and potential energy entering and leaving at the barrel inlet and outlet planes.
3. Integrate the turbulent dissipation rate over the water volume in the barrel.

All of these methods are challenging because of the relatively small losses in comparison to the kinetic and potential energy of the flow. The tilt angle needed to convert gradational potential energy to kinetic energy at a rate necessary to make up for turbulent losses and keep the water depth constant in the barrel constant is generally very small. Accurate determination of the required tilt angle requires very accurate resolution of the free surface, within a millimeter or less in the tests conducted, and the computational resources needed for such an accurate resolution of the height of the free surface begin to become unreasonably large. The problem with the second approach of taking the difference

between energy leaving at the outlet plane and entering at the inlet plane is that these quantities are nearly equal, and there is a loss of precision in subtracting nearly equal numbers. If the computation of mechanical energy transport is accurate to approximately 3 decimal places (error less than 0.1 %) and the energy in and out are close to equal in the first two decimal places, then subtracting these numbers leaves a result that is uncertain in the first decimal place. Integrating the turbulent dissipation rate over the volume may offer the most accurate way to determine losses from a numerical perspective because it sums up the small quantities of interest.

**Table 2.1 Comparison of flume tilt needed to balance flow losses for three tested CFD analysis methods and the value obtained using Manning's formula for fully developed flow**

Method	Tilted Flume	Horizontal Flume		Manning's (Fully-Developed)
	Automation (CFD Simulation)	Turbulent Dissipation	Energy of Flow	
Slope (Radians)	$7.01 \times 10^{-4}$	$7.48 \times 10^{-4}$	$7.21 \times 10^{-4}$	$5.72 \times 10^{-4}$
Slope (Degrees)	0.0401	0.0428	0.0413	0.0328
Percentage Difference w.r.t Manning's (Fully-Developed)	22.5%	30.7%	25.9%	-

**Error! Reference source not found.** shows typical results in obtaining a flume tilt angle that corresponds to balancing losses in the culvert barrel in the flume. The results for the three approaches using CFD agree within ten percent, which was expected given the small losses compared to the potential and kinetic energy of the flow. Results were also compared to a value obtained by taking a value of Manning's n parameter from a chart for the type of culvert and approximate flow conditions. The Manning's formula assumes fully developed flow conditions. However, the flow conditions in the experimental flume were not fully developed and not uniform over the cross-section. Conditions within the experimental culvert barrel are not sufficient to meet the assumption for application of Manning's formula for two reasons. First, the culvert barrel is not long enough for the flow to become fully developed. Second, the diffuser exit geometry is not symmetric with respect to the barrel, and the effects of the exit region geometry extend more than half the distance upstream to the barrel entry as shown in the cross section velocity distributions in Figure 2.9. Streamlines through the culvert flume are plotted in Figure 2.8 showing that the flow cannot follow the sharp angled expanding wall in the asymmetric diffuser section and separates creating a large recirculation zone in the diffuser. The differences in this flow pattern and the fully developed symmetric flow assumption used with Manning's formula for obtaining the losses yield a higher loss than that obtained from Manning's formula by about 25 percent. The water surface height in the CFD computation matched surface height of the laboratory experiment within five percent, and the change in surface height due to losses matched that obtained in the laboratory to within less than one percent. Therefore the CFD computation appears to be a good way to compute flow patterns and losses in culverts that may not correspond to the ideal conditions for application of Manning's formula.

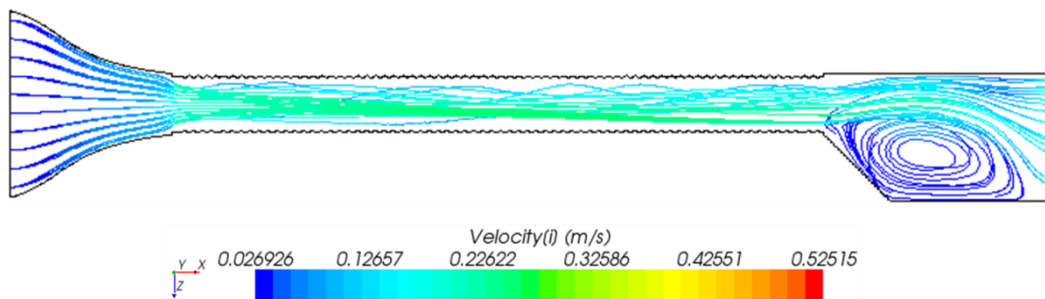


Figure 2.8: Streamlines through culvert flume showing separation of flow in the exit section of the culvert with a large recirculation zone

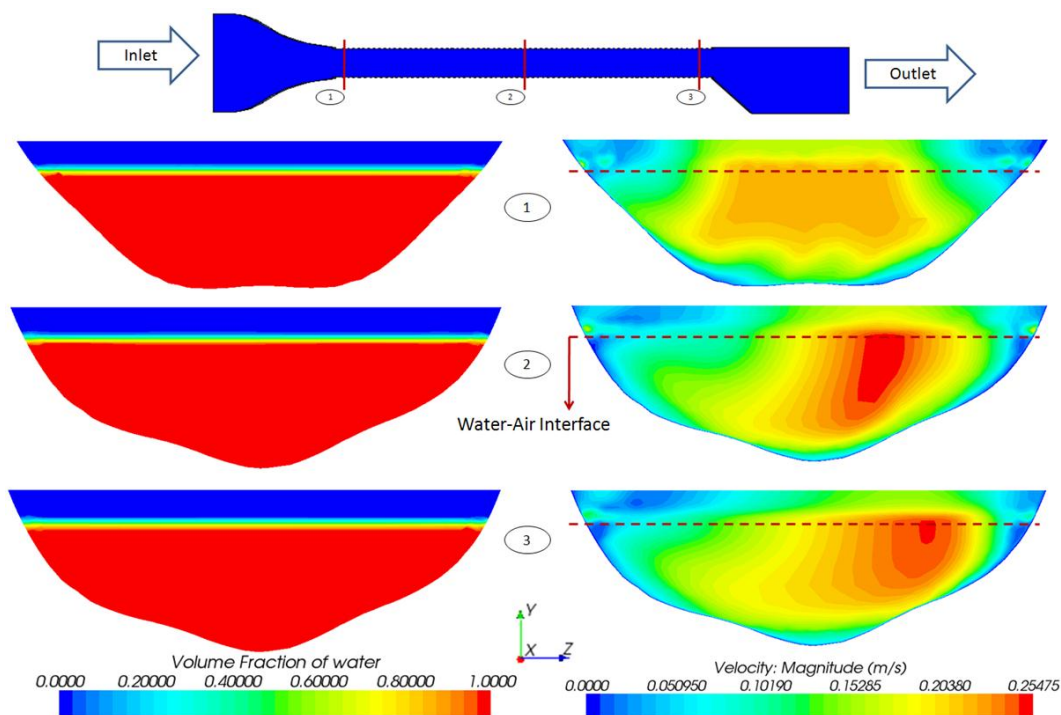


Figure 2.9: Water height and velocity distributions in culvert cross sections showing effects of the asymmetric exit geometry upstream halfway between the culvert barrel entry and exit

### 2.1.5 Test CFD Analysis of Wind Loads on Single Bridge Decks

This subject was not explored in the recent quarter.

### 2.1.6 References

- (1) Van Rijn, L. C. *Sediment pickup functions*. J. Hyd. Eng. ASCE 1984, 110(10)

- (2) Cobb, M., and T.R. Keen, *Coehsive Sediment Entrainment Rate Functions: Expanding and Quantifying Their Parameterizations*, Naval Research Laboratory, Report NRL/MR/7320—08-9069, 2008.
- (3) Lottes, S.A., *Hydraulics and Scour Modeling Notes*, unpublished, Argonne National Laboratory, 2010.

## 3 Computational Multiphysics Mechanics Technical Section

### 3.1 Technical Background

Computational multiphysics mechanics is used for the assessment of many safety issues that are of major concern to USDOT and FHWA. Computational multiphysics mechanics refers to the combination of several traditional computational areas, such as structural mechanics and fluid mechanics (aerodynamics and hydrodynamics), that can be solved in a coupled fashion to properly treat the interactions. These include but are not limited to the following areas: (1) multiphysics analysis of stay cables, (2) transient dynamic analysis of highway bridges to traffic and wind loadings, and (3) stability of bridges with piers in scour holes.

Bridge failure due to wind has been observed as far back as 1823. The latest concept for bridge design is the cable-stayed bridge, which has been firmly established as an efficient and cost-effective structure. Bridge stay cables, however, have exhibited large amplitude vibrations as a result of wind loadings, sometimes in combination with rain. A potential application for TRACC's computational resources centers on modeling and simulation of the structural response of bridge stay cables to aerodynamic loading, which leads to aerodynamic-structure coupling, and this requires a multiphysics approach — that is, the simultaneous use of computational structural mechanics and computational fluid dynamics simulation methods. This approach will lead to the long-term goal of studying the dynamic response of bridges to simultaneous traffic and aerodynamic loadings.

In recent years, attempts have been made to model this problem both in the laboratory and on the computer. Several wind tunnel tests have been conducted in North America in an effort to better understand the mechanisms involved in this problem so that better or more efficient mitigation methods can be established. While some tests have focused on the simulation of rain and/or water rivulets on the surface of the cable and its influence on stability, others have concentrated on dry cable behavior, looking at the response to vortex shedding and galloping and measuring pressure fluctuations



and the distribution of the cable surface. Although there has been some experimental work looking at the effectiveness of aerodynamic surface treatments, this research has largely been performed by cable suppliers, and the results are proprietary. To better understand wind effects on cables, computational and simulation methods are needed to efficiently evaluate the direct effects of wind loads on cables under a range of expected wind conditions (turbulence intensity, speed, and direction) and to assess the efficacy of various mitigation methods (including surface treatment).

As an extension of the above cable problem, it is also possible for undesirable cable vibrations to result from wind-induced motion of the cable anchorages. In this case, the anchorage motion can be the result of traffic on the bridge, wind loading on the bridge deck and/or tower(s), or combinations of the two. Here, cable vibration is not primarily the result of wind load directly on the cable, but on some other part of the structure and feeding energy into the cable. Where there is a relatively close match between deck or tower and cable frequencies or multiples thereon, large cable vibrations can result. To better understand the nature and extent of this problem, computational and simulation methods are needed to efficiently model the anchorage motions resulting from buffeting and other wind effects on the main structure and assess the impact of these motions on cable stability.

Computational fluid dynamics is currently being used to analyze riverbed scour to determine the depth and shape of the scour hole around bridge piers and abutments. Once these profiles have been determined, the critical question is: Will the bridge structure remain stable or will the bridge collapse? To answer this question, a structural stability analysis must be performed for the evolving scour hole shapes to find the depth and shape at which structural failure occurs. This analysis requires a multiphysics-capable code that can capture the fluid-structure interaction between the moving river and the bridge pier and the soil-structure interaction between the embedded pier and riverbed soil. The computational structural mechanics code LS-DYNA® has these capabilities and, thus, will be used for the bridge stability analysis.

## 3.2 Technical Approach

Many new research areas of interest to the DOT require the use of advanced computing technologies. Modeling and simulation in three dimensions is the only way to understand the complex interactions among bridge structures, wind, and river flow. This understanding can only be accomplished with the use of teraflop computers, such as the TRACC cluster computer. Once this understanding is available and the computational multiphysics mechanics methods are validated for prototypic applications, then current designs can be evaluated and modified to produce safer and more reliable structures, and future bridges can be designed — initially — with greater structural integrity and more confidence in safety margins.

The technical approach to this project is to apply computational multiphysics mechanics modeling and simulation techniques to three areas of interest to DOT: (1) transient response of stay cables to wind and parametric loading, (2) dynamic response of stay-cable bridges to traffic and wind loading, and (3)

stability of bridges with piers in scour holes. This research will be conducted in collaboration with staff from Turner Fairbank Highway Research Center.

### 3.3 First-Year Tasks

This quarterly report describes the work done on the project's Computational Multiphysics Mechanics tasks. Also described are the results of a short feasibility study on the application of the multimaterial-Arbitrary Eulerian Lagrangian approach to a new problem-of-interest of TFHRC, which is the transport of salt spray generated by truck tires onto the exposed underside steel beams in bridge underpasses.

#### 3.3.1 Hybrid Multiphysics Analysis of Stay Cables

##### 3.3.1.1 Develop user subroutine for wind loads

This subject was not explored in the recent quarter.

##### 3.3.1.2 Benchmark hybrid approach against analytical solutions and experiments

This subject was not explored in the recent quarter.

#### 3.3.2 Multiphysics Analysis of Stay Cables

##### 3.3.2.1 Develop 3D multiphysics models for a single stay cable

This subject was not explored in the recent quarter.



### 3.3.3 Traffic and Wind Loading of Stay Cable Bridges

Some of the work reported in this section was previously performed with USDOT/RITA funding. Subsequently, this research area became part of the current research sponsored by Turner Fairbank Highway Research Center. To introduce the work and maintain future continuity, both the earlier work and new work are included in this first quarterly report.

#### 3.3.3.1 Develop vehicle models for traffic loading

Long span cable stayed bridges are usually characterized by numerous, closely spaced low natural frequencies below 1 Hz. For a particular combination of cable and deck frequencies, large amplitude cable vibrations due to parametric excitation may occur even for considerably low traffic, wind or seismic loading. The mechanism of parametric excitation is well described theoretically for simple academic cases. However, due to the complexity of the parametric resonance phenomenon, analysis of bridges for this purpose is only possible by using explicit Finite Element (FE) simulations.

This study presents a FE analysis of the Bill Emerson Memorial Bridge subject to seismic and traffic loading and their influence on vibrations of the cables. The development of the FE model of the bridge for use with the LS-DYNA® code is described. The model was validated by comparison of calculated natural frequencies with experimentally determined values.

The bridge was subjected to seismic loading registered during the Northridge earthquake. This simulation revealed large oscillations of the cables that were induced by the tower lateral vibrations. However, the vibrations did not lead to excessive stresses in cables.

A simplified model representing the AASHTO HS 20-44 truck was also developed. The truck model was used to simulate traffic loading on the bridge. The interaction between the truck and the bridge deck was defined through a special LS-DYNA algorithm – RAIL. In this paper, cases with one and twenty trucks on the bridge were examined. No excessive cable vibrations due to traffic loading were observed.

##### 3.3.3.1.1 Introduction

Cable stayed bridges are characterized by a high ratio of span length to material weight. This property assures their high cost effectiveness, but at the same time it brings additional design challenges. Low mass per unit length of cables (50 – 150 kg/m) together with low structural damping (0.03 – 0.1 % of critical) increase their susceptibility to different types of vibrations that can accelerate deterioration of the bridge condition.

The vibrations in a cable stayed bridge may be considered as either direct or indirect vibrations. Direct vibrations can be caused by rain and wind loads on cables, and in particular by buffeting, vortex-shedding, wake effects and galloping. Indirect vibrations in the cables can be induced by vibrations of the deck and the tower caused by the wind, seismic or traffic loads. When certain conditions in the bridge structure are met, indirect vibrations can lead to disproportional amplification of the cable oscillations perpendicular to the cable axis. As defined in (1) and (2), susceptibility to this type of vibrations may be assessed by calculation of the modal frequency ratio given by Equation:

$$r_m = \frac{\Omega_m}{\omega_1} \quad (3.3.1)$$

Where:

$\Omega_m$  –  $m^{\text{th}}$  modal frequency of the bridge (global)

$\omega_1$  – fundamental frequency of cable (local)

For the cases when  $r_m = 1$  and  $r_m = 2$  vibrations may easily enter instability regions and parametric resonance of the cables may take place. This phenomenon is caused by nonlinear coupling of vertical (in line of axis) and lateral (perpendicular to axis) vibrations in the cable. Parametric excitation is especially dangerous for the case  $r_m = 2$  since the instability region can be entered even for low amplitudes of traffic induced vibrations (3). Although parametric resonance is well understood theoretically (1), (3), (4), (5) appropriate analysis of the bridge structures in combination with various cases of live and seismic loadings can be only achieved by thorough FE analysis (2).

In this paper, the Bill Emerson Memorial Bridge is examined for susceptibility to parametric excitations in cables due to seismic and traffic loading. Development of the FE models of the bridge and the AASHTO HS 20-44 truck for use with the LS-DYNA commercial code is described in detail. The modeling approach resulted in very efficient and stable FE calculations and can be used for analysis of other cable stayed bridges.

#### **3.3.3.1.2 Parametric Excitation Phenomenon**

To examine LS-DYNA capability to capture parametric resonance, a simple cable-mass model was studied as described in (3) and shown in Figure 3.3.1. The model consists of a cable with initial length,  $L$ , uniform mass per unit length,  $\rho A$ , and axial elastic stiffness,  $EA$ . The cable was under initial tension,  $T_0$ . An additional spring element was modeled to represent bridge deck stiffness,  $k$ . Table 3.1 lists the material properties and initial conditions for the analyzed system.

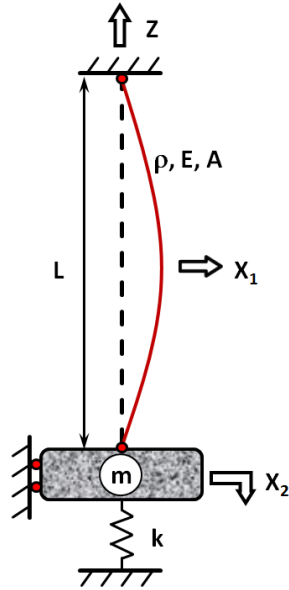


Table 3.1: Model properties

Quantity	Assumed value
$L$	40 m
$\rho A$	0.25 kg/m
$EA$	6,000 N
$T_0$	101 N
$X_1(0)$	0.001 m
$X_2(0)$	0.1 m

Figure 3.3.1: Dynamic model of stay cable

As defined in (3), the natural frequency of a tensioned cable is obtained from the equation:

$$\omega_s = \left( \frac{s\pi}{L} \right) \sqrt{\frac{T_0}{\rho A}}; \quad (s=1,2,\dots,n) \quad (3.3.2)$$

And the natural frequency of the vibrating mass (deck) is given by:

$$\omega_2 = \frac{EA}{mL} + \frac{k}{m} \quad (3.3.3)$$

By substituting values from Table 3.1 into equations (3.3.2) and (3.3.3) for  $s=1$ , the ratio  $r_m$  was calculated to be 2.003. Thus, parametric excitation is expected in the system.

Response of the cable in horizontal and vertical directions is described by following equations (3):

$$\ddot{X}_1 + \omega_1^2 \left[ 1 + \frac{X_2}{z_o} + \frac{\pi^2 X_1^2}{4Lz_o} \right] X_1 = 0 \quad (3.3.4)$$

$$\ddot{X}_2 + \omega_2^2 X_2 + \frac{AE}{mL} Kz_o X_1^2 = 0 \quad (3.3.5)$$

The vibrations of the mass (deck) are nonlinearly coupled with lateral vibrations of the cable. Figure 3.3.2 shows numerical solution to the system of equations (3.3.4) and (3.3.5). Figure 3.3.2 a shows displacement history of the mass while Figure 3.3.2 c shows lateral displacement of the cable mid-span. It can be noticed that the amplitude of the cable vibrations increases drastically from initial perturbation of 0.001 m. The maximum amplitude of these vibrations  $\sim 0.8$  m occurs for each minimum of mass vibration amplitude. The mass vibration shows beating characteristic.

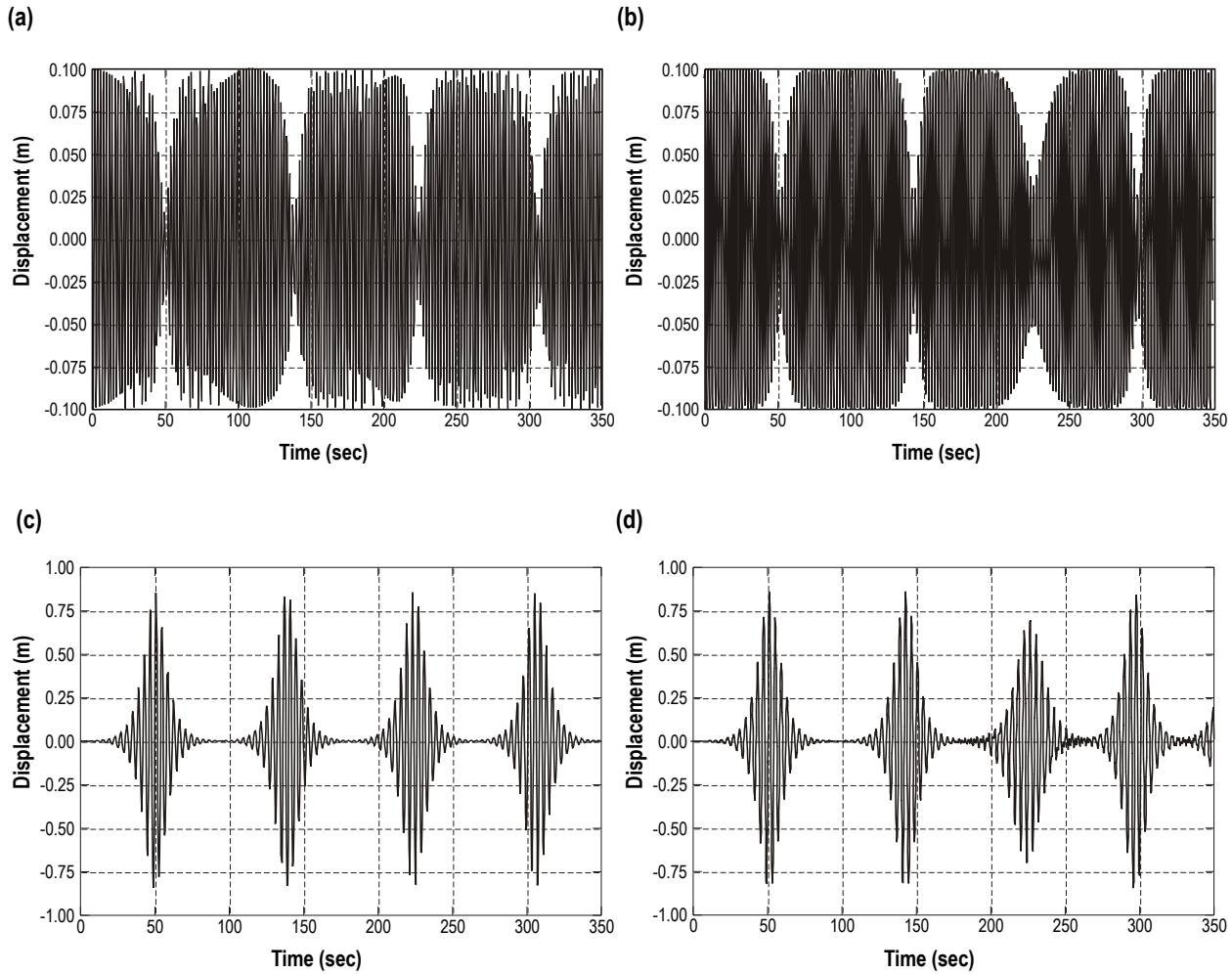


Figure 3.3.2: Comparison of Finite Element solution to analytical solution for cable parametric vibrations:

(a) in line with exciting force – analytical (b) in line with exciting force – Finite Element

(c) perpendicular to exciting force – analytical (d) perpendicular to exciting force – Finite Element

The LS-DYNA beam element (formulation 6; discrete beam/cable) with cable material (MAT\_071) was used to model the system. The material allows for introducing initial tension in the cable. Two parameters were crucial for obtaining the desired behavior of the cable elements in the numerical simulations: time at which the tension load increases (TRAMP) and time for which the pre-tensioning force is held (TMAXFO).

Figure 3.3.2 b and d are plots for vertical displacement of the deck and horizontal displacement of the cable obtained from the simulation. The cable and the mass exhibit very similar behavior to those described by the analytical solution of equations (3.3.4) and (3.3.5), which are shown in Figure 3.3.2 a and c. Thus it can be concluded that the LS-DYNA beam element with formulation 6 is capable of capturing the parametric excitation in the stay cables.

### 3.3.3.1.3 *Finite Element Model of Bill Emerson Memorial Bridge*

The FE model of the Bill Emerson Memorial Bridge was developed to study the cable vibrations under seismic and traffic loading. It is a cable-stayed bridge connecting Missouri's Route 34 and Route 74 with Illinois Route 146 across the Mississippi River. A photograph of the bridge and its location on the map is shown in Figure 3.3.3 a and b, respectively.



Figure 3.3.3: Bill Emerson Memorial Bridge

The bridge has a total length of 1206 m (3956 ft). It consists of one 350.6 m (1150 ft) long main span, two 142.7 m (468 ft) long side spans, and one 570 m (1870 ft) long approach span on the Illinois side. Due to flexible connection between the approach and the main bridge, the approach was not modeled here. Carrying two-way traffic, the bridge has four 3.66 m (12 ft) wide vehicular lanes plus two narrower shoulders. The total width of the bridge deck is 29.3 m (96 ft).

To study bridge vibrations it is usually required to simulate a period of one minute or more of a real time. This is considered to be a long lasting event for an explicit Finite Element analysis. For this type of analysis, the increment at which the calculations are performed (i.e., timestep) need to be high enough and the number of elements need to be kept reasonable, so that the computations aren't too

expensive. This usually requires a reduction in the details of the model and appropriate modeling of the relevant elements of the real bridge. Figure 3.3.4 shows the most crucial elements of the bridge structure that were included in the FE model.

Solid elements with one integration point were used to model the towers (Number 1 in Figure 3.3.4). The concrete was simulated with linear elastic type of material (MAT\_001).

The bridge deck was composed of two longitudinal steel girders located on the sides, transverse floor beams, and precast concrete slabs. A concrete barrier was located in the center of the bridge, and two railings and additional concrete barriers were designed along the edges of the deck.

The deck slab (2) was built of two layers of reinforced concrete: 279 mm thick bottom part and 76 mm thick upper surface. In the FE model the deck was represented with one layer of shell elements. A special integration scheme through the thickness of shells was used to account for the multiple materials and composite structure of the slab. This approach significantly reduces the number of elements used in the model but still correctly models the flexural and torsional behaviors of the deck.

The cross beams (3) under the deck slab and the main steel girders (4) running on the edges of the deck were modeled using shell elements with a piecewise linear plasticity material model. The modeled cross beams were connected to the girders using a spot-weld type of connection. The deck slab was connected to the beams using rigid links representing dowels. This approach avoids over stiffening of the structure when all the nodes in adjacent members are merged.

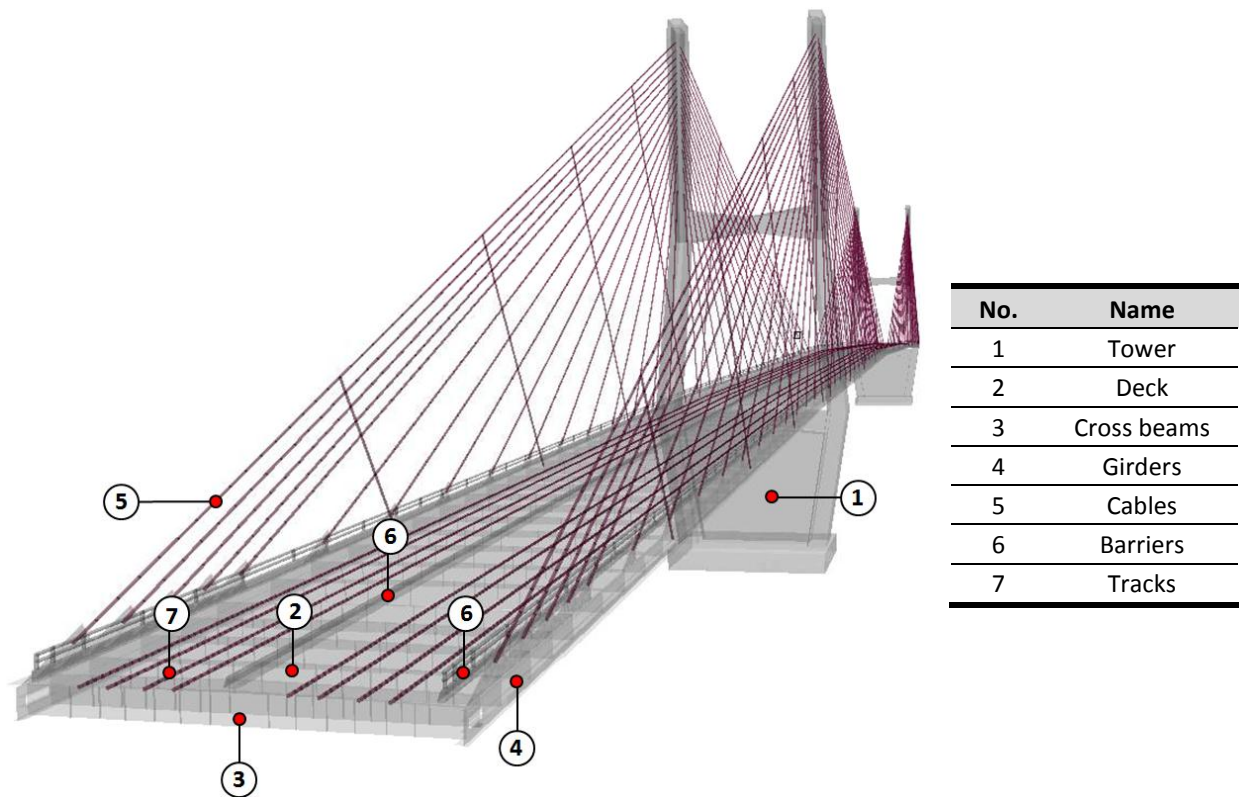


Figure 3.3.4: FE model of Bill Emerson Memorial Bridge – view of the deck structure

In the Bill Emerson Memorial Bridge, each cable (5) consists of from 19 to 54 separate strands (6); each strand was 15.7 mm in diameter. Overall there are 128 cables with 32 different cross sections and pre-tensioning forces. The multiple strands were modeled in the FE model with one line of beam elements (with element formulation 6) with equivalent properties of the bundle of strands. Figure 3.3.5 shows numbering of the 32 different cables. Their averaged properties were calculated and presented in Table 3.2.

The total number of elements in the model was nearly 250,000 out of which around 172,000 were shell elements. The smallest shell and solid elements had their edge size around 0.12 m. This resulted in a stability timestep of 2.45E-5 sec for the explicit calculations.



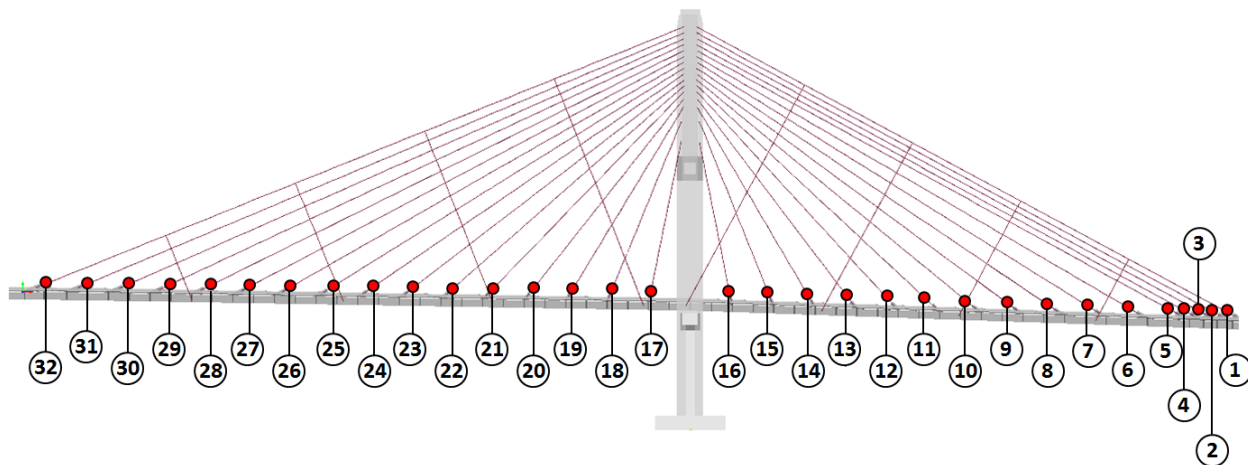


Figure 3.3.5: FE model of Bill Emerson Memorial Bridge with numbering of the stay cables

Table 3.2: Averaged properties of the cables in FE model of Bill Emerson Memorial Bridge (6)

Cable No	Diameter (m)	Length (m)	Mass per unit length (kg/m)	Average Tension (kN)	1 <sup>st</sup> Natural Frequency (Hz)	1 <sup>st</sup> Natural Frequency – with ties (Hz)
1	0.1014	158.86	63.42	7910.75	1.11	5.61
2	0.1014	154.84	63.42	8304.47	1.16	5.75
3	0.0976	150.84	58.79	7809.66	1.20	5.79
4	0.0926	147.02	52.90	5564.54	1.10	5.15
5	0.0905	143.02	50.54	5457.16	1.17	5.22
6	0.0884	132.86	48.19	4965.15	1.20	5.10
7	0.0840	122.68	43.48	5378.06	1.43	5.57
8	0.0840	112.77	43.48	5098.03	1.51	5.41
9	0.0817	103.11	41.12	3680.18	1.45	4.70
10	0.0769	93.49	36.41	3878.05	1.74	5.09
11	0.0769	84.25	36.41	3697.04	1.89	4.92
12	0.0756	75.45	35.24	3140.91	2.01	4.50
13	0.0717	66.95	31.71	2477.82	2.08	4.07
14	0.0662	58.96	27.07	1843.99	2.21	3.93
15	0.0632	51.77	24.64	1200.66	2.13	4.37
16	0.0602	44.25	22.37	1216.16	2.63	4.40
17	0.0602	43.57	22.37	1118.01	2.56	2.72
18	0.0632	50.47	24.64	1372.48	2.33	3.11
19	0.0662	57.21	27.07	1796.99	2.25	3.65
20	0.0676	64.85	28.17	1982.16	2.04	3.97
21	0.0744	73.06	34.06	2949.24	2.01	3.70



<b>22</b>	0.0756	81.66	35.24	3418.33	1.90	4.10
<b>23</b>	0.0769	90.71	36.42	3960.13	1.81	4.43
<b>24</b>	0.0805	100.17	39.95	4001.10	1.57	4.31
<b>25</b>	0.0840	109.74	43.48	5288.77	1.58	4.79
<b>26</b>	0.0840	119.60	43.48	5265.81	1.45	4.81
<b>27</b>	0.0894	129.68	49.29	5136.45	1.24	4.48
<b>28</b>	0.0916	139.82	51.72	5165.87	1.13	4.40
<b>29</b>	0.0926	150.00	52.90	5589.46	1.08	4.53
<b>30</b>	0.0966	160.10	57.61	7770.74	1.14	5.13
<b>31</b>	0.1015	170.43	63.42	8624.37	1.08	5.14
<b>32</b>	0.1015	180.94	63.42	7550.08	0.95	4.82

#### ***3.3.3.1.4 Finite Element Model Validation***

One of the methods for validating numerical models of bridges is to analyze the natural frequencies and the free vibration mode shapes. Such data for the Bill Emerson Bridge was available in an earlier published report - (6). The eigenvalue analysis was performed on an 8 core machine with double precision MPP-DYNA 971 r5.0. The simulation used ~25 GB of RAM memory and took approximately 3 hours. The first seven global natural frequencies and mode shapes are shown in Figure 3.3.6.

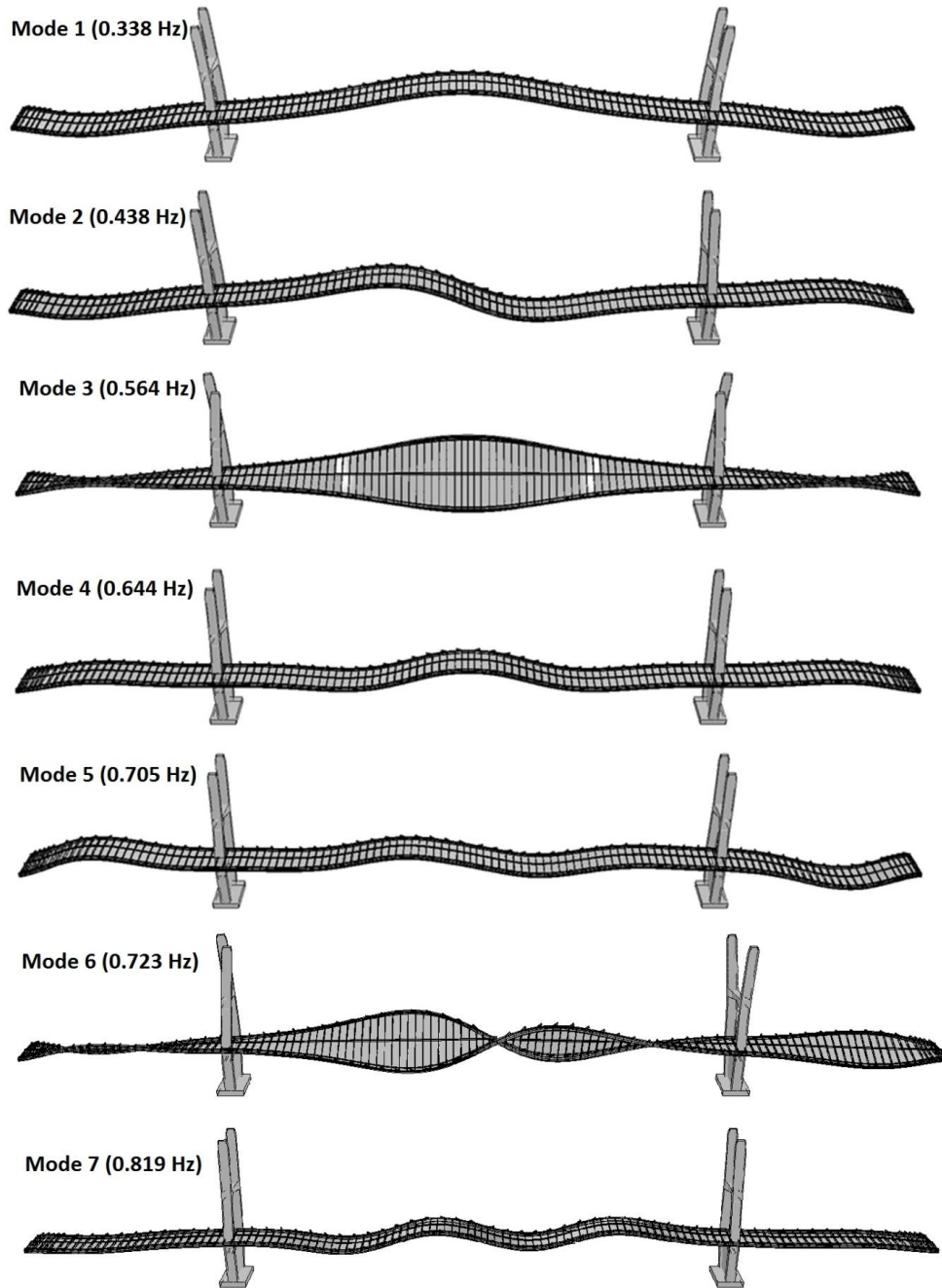


Figure 3.3.6: First seven global mode shapes for FE model of the Bill Emerson Memorial Bridge

The comparison between experimental data and the numerical values for the lowest natural frequencies is shown in Table 3.3. For the extracted natural frequencies, the relative errors were very low for bending modes from 0.0 to 1.1 % and were in acceptable range for torsional modes (3 and 6) from 4.1 to 6.7 %. The first seven natural frequencies of the bridge are less than 1 Hz. The modal frequency ratio  $r_m$  for these values is less than one.

Table 3.3: Comparison of natural frequencies of the FE model with experimental values

Mode number (type)	Experiment	FE model	Relative Error (%)
1 (bending)	0.338	0.338	0.00
2 (bending)	0.438	0.438	0.00
3 (torsional)	0.588	0.564	4.08
4 (bending)	0.650	0.644	0.09
5 (bending)	0.713	0.705	1.12
6 (torsional)	0.775	0.723	6.71
7 (bending)	0.825	0.819	0.73

### 3.3.3.1.5 Seismic Loading Analysis

The Northridge earthquake (1994) vertical acceleration history was used to simulate seismic loading on the bridge. Since Pier 2 (west tower) rests on rock while Pier 3 (east tower) and Pier 4 foundations are supported on two separate caissons it was assumed that the acceleration is directly applied to the bridge towers' bases. Figure 3.3.7 a shows the vertical acceleration history registered during the Northridge earthquake. Figure 3.3.7 b shows the Fourier Transform of that acceleration history. A wide frequency bandwidth can be noticed in the low frequency range (0 – 4 Hz) where the majority of the natural frequencies of the bridge (global and local for cables) are located.

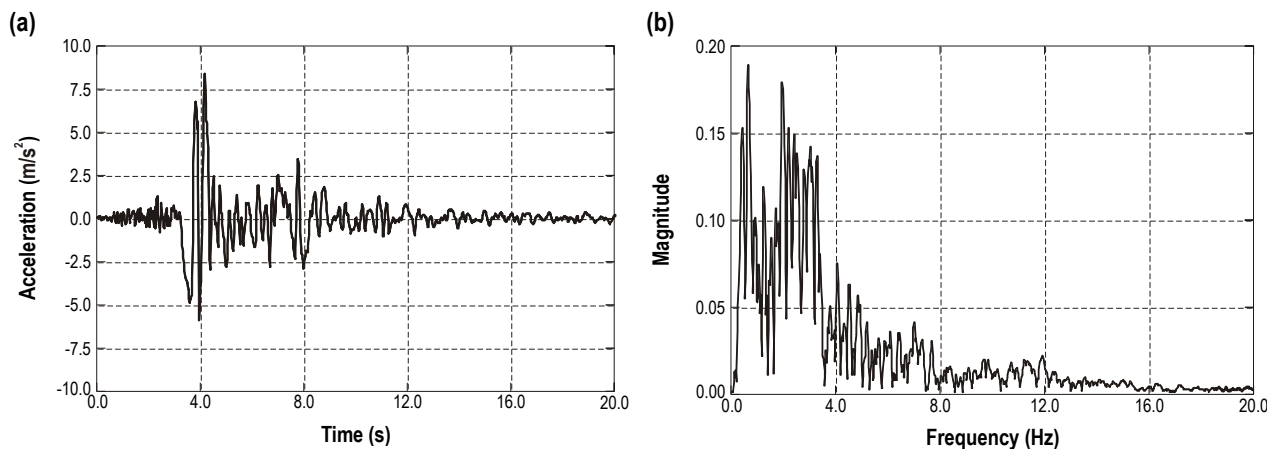
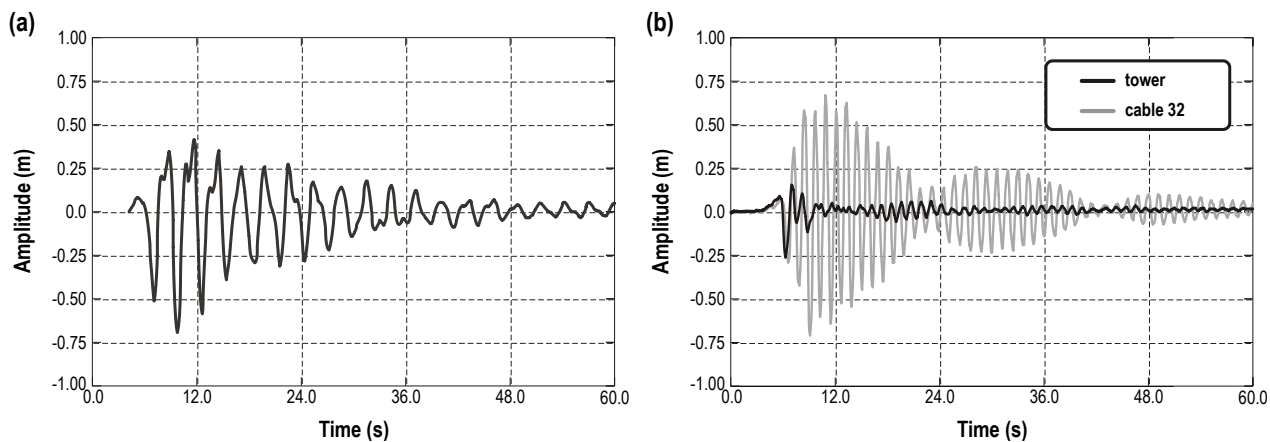


Figure 3.3.7: Northridge earthquake (a) vertical acceleration history (b) Fourier Transform of the history



**Figure 3.3.8: Response of the bridge model to the Northridge earthquake**  
**(a) Deflection history at the mid-span (b) Lateral vibrations of tower and cable 32**

Figure 3.3.8 shows the response of the bridge to the applied seismic load. Figure 3.3.8 a presents the vertical motion of the bridge deck at the mid-span. The maximum displacement ranged from -0.69 m to 0.4 m. Significant lateral oscillations in the cables were induced by lateral vibrations of the pylon (see Figure 3.3.8 b). While the tower vibrations were quickly damped out, the vibrations of the cables were significantly amplified. Their peak-to-peak amplitude reached ~1.4 m. However, the stresses in the cables induced by these vibrations do not reach the yield state.

#### 3.3.3.1.6 Traffic Loading Analysis

Interaction between the simplified model of the vehicle with the bridge structure was performed in LS-DYNA using keywords RAIL\_TRACK and RAIL\_TRAIN (7). A track represents the path built of beam elements that is followed in the simulation by a generalized vehicle. The elements were embedded in the deck structure (see Figure 3.3.4). The null material (MAT\_009) was used for these beams to not introduce additional stiffness to the bridge deck. LS-DYNA interpolates a smoothed vehicle path from the piecewise linear beam elements to avoid spurious roughness resulting from element discretization.

All the nodes representing contact patches of the wheels are introduced in the RAIL\_TRAIN definition. The interaction between the simplified wheels and the track is invoked by a penalty contact. The road roughness can be defined in the interaction as well. The roughness can either be taken from the field measurements or generated numerically. For that purpose, the road surface was considered to be a random deviation from a perfect flat road surface. In the literature (8), it is frequently characterized by the following equation:

$$r(x) = \sum_{k=1}^N \sqrt{4A_r \left( \frac{\pi k}{L\omega_0} \right)^{-2} \frac{\pi}{L} \cos \left( \frac{\pi k}{L} x + \varphi_k \right)} \quad (3.3.6)$$

Where:

$A_r$  — is the roughness coefficient in  $\text{m}^3/\text{circle}$ , assumed  $256 \times 10^{-6}$  for poor road conditions (9)

$\omega_0$  — is the discontinuity frequency taken as  $\frac{1}{2} \pi$  circles/m

$L$  — is the length of the bridge

$\varphi_k$  — is the phase angle for the  $k^{\text{th}}$  frequency generated randomly from the range  $(0 - 2\pi)$

The data points were generated every 0.1 m of the road. The roughness profile was characterized by peak-to-peak amplitude of  $\sim 35$  mm.

The smallest finite elements in the model currently have an edge length of approximately 0.12 m. Detailed FE models of vehicles would require even smaller size of elements to appropriately model truck tires. Moreover, including multiple vehicle models on the bridge would significantly increase the number of elements and contact definitions. The RAIL algorithm in LS-DYNA allows solving this problem by modeling only simplified vehicles. That way the flexible suspension of real vehicles can be simulated. For this study, a truck was modeled as a 3D mass-spring-damper system as shown in Figure 3.3.9. The vehicle has mass and size properties representing the AASHTO HS 20-44 truck. The HS 20-44 truck is considered as a set of forces only (rigid-like vehicle). Here the truck was modeled with flexible suspension to allow for appropriate analysis of dynamic interaction with the bridge.

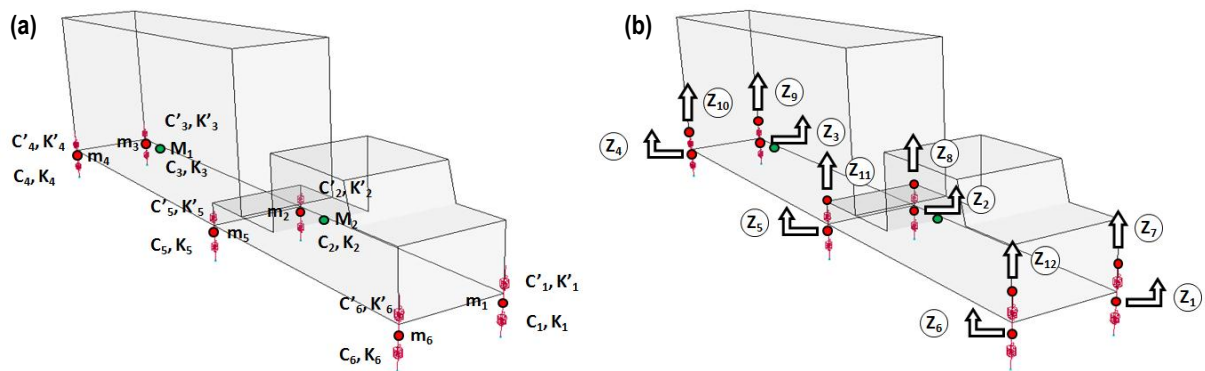


Figure 3.3.9: Simplified FE model of the AASHTO HS 20-44 truck

The vehicle Finite Element model consists of eight rigid masses which represent the tractor, semi-trailer and six wheels. The tractor and semi-trailer are each assigned 3 DOFs, corresponding to the vertical displacement (Z) at the mass center, pitching rotation ( $\theta$ ) and rolling rotation ( $\phi$ ). Each wheel is modeled as a lumped mass with only vertical displacement (z). There are a total of 11 independent DOFs in this

model. Based on the Florida DOT loading truck (10), which closely matches the mass and size of the AASHTO design truck, springs and dampers were used to model the suspension. The properties of the model are listed in Table 3.4.

**Table 3.4: Vehicle model stiffness and mass properties (10)**

Property	Value
Mass(tonne)	$m_1=m_6=0.482$ , $m_2=m_5=0.670$ , $m_3=m_4=0.934$ , $M_1=5.99$ , $M_2=22.56$
Mass moment of inertia (ton-mm <sup>2</sup> )	$I_{p1}=3.21 \times 10^7$ , $I_{p2}=5.06 \times 10^7$ , $I_{r1}=1.91 \times 10^6$ , $I_{r2}=1.08 \times 10^7$
Tire suspension (N/mm)	$k_1=k_6=2250$ , $k_2=k_3=k_4=k_5=8000$
Suspension stiffness (N/mm)	$k_1'=k_6'=4000$ , $k_2'=k_3'=k_4'=k_5'=8000$
Tire damping (N-t/mm)	$c_1=c_2=c_3=c_4=c_5=c_6=20$
Suspension damping (N-t/mm)	$c_1'=c_2'=c_3'=c_4'=c_5'=c_6'=20$

Two cases of traffic loading were investigated: with one truck and with twenty trucks (ten in each direction). A constant velocity of 25 m/s (56 mph) was assigned to the vehicles. The trucks were spaced 20.5 m apart what gave ~3.0 second interval between them. This loading pattern corresponds to the first natural frequency of the bridge. Figure 3.3.10 a shows the deflection of the deck at the mid-span.

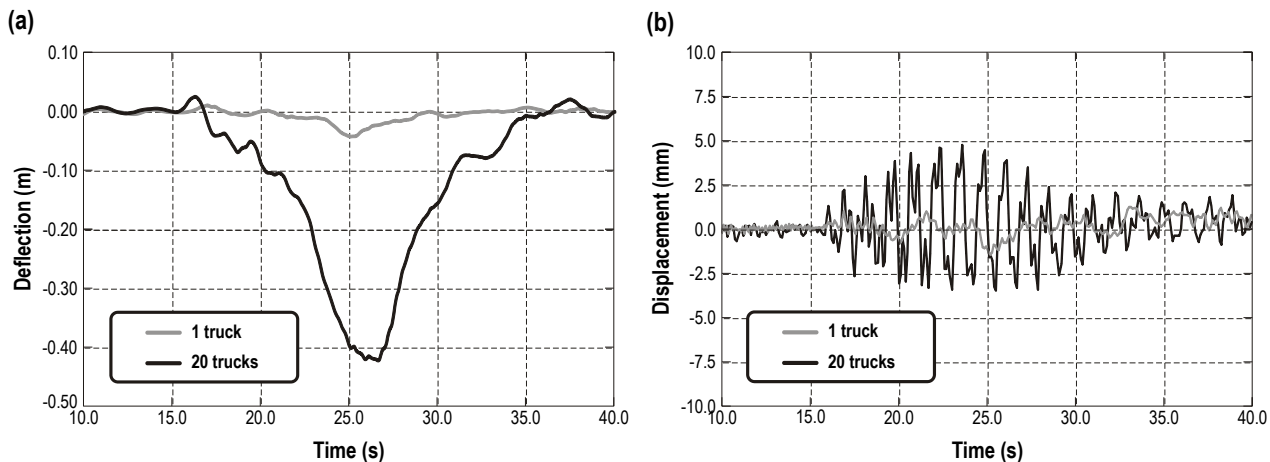


**Figure 3.3.10: Response of the bridge to the traffic loading**  
**(a) Deflection history at the mid-span (b) Lateral vibrations of cable 32**

The maximum deflection under one truck was ~ 0.04 m. The maximum deflection under twenty trucks was ~0.43 m. Figure 3.3.10 b shows vibrations of the longest cable (number 32) in the lateral direction. The amplitude of the vibrations was very small and reached a maximum of 10 mm for the case with 20 trucks.

#### 3.3.3.1.7 Conclusions

Parametric excitation of the cables in cable-stay bridges may occur in real life when the modal frequency ratio approaches 2. This comes from the non-linear coupling of axial and out-of-plane vibrations of the cables. To capture this behavior, the analysis of cables cannot be separated from the deck and towers.

It has been shown in the study that LS-DYNA software can be used to appropriately model the cables in cable stay bridges and has capabilities to capture parametric resonance.

A Finite Element model of the Bill Emerson Memorial Bridge was built to study the influence of seismic and traffic loading on stay cable vibrations. For the lowest natural frequencies of the bridge, modal frequency ratio was calculated to be in the safe region  $r_m < 1$ . The cross-tie vibration suppression system increases the natural frequencies of the cables, thus, decreasing the possibility for parametric excitation.

The bridge was subjected to the Northridge earthquake acceleration history. Transverse oscillations ranging from -0.71 m to 0.67 m were induced in the longest cable. These vibrations did not lead to excessive stresses in cables. The maximum deflection of the deck at the mid-span was 0.69 m.

Traffic loading in the form of twenty AASHTO HS 20-44 trucks traveling in opposite directions (ten in each direction) deformed the mid-span of the deck by 0.43 m, and produced low level cable lateral vibrations with amplitude of 10 mm for the longest cable.

#### 3.3.3.1.8 References

- (1) Nayfeh A. H., Mook D. T., Nonlinear Oscillations, Wiley Classic Library, ISBN 0-471-12142-8, 1995.
- (2) Stoyanoff S., Pridham B., Irwin P. Gamble S., Analysis and Design of Vibration-Suppressing Systems for Stay Cables, Wind Induced Vibration of Cable Stay Bridges Workshop, St. Louis, MO, 2006, <http://www.modot.mo.gov/csb/documents/14-AnaysisandDesignofVibration-SuppressingSystemsforStayCables.pdf>, last accessed: 07-15-2010.
- (3) Sun, B. W., Wang Z. G., Ko J. M., Nr Y. Q., Cable oscillation induced by Parametric Excitation in Cable-Stayed Bridges, Proceedings of International conference on advances in structural Dynamics, , p.533-560, Hong Kong, 2000.
- (4) Fujino, Y. W., An experimental and analytical Study of auto Parametric Resonance in 3DOF Model of Cable Stayed Beam, International Journal of Nonlinear Dynamics, Vol. 4, pp 111-138, 1993.
- (5) Zhang C.Y., Zhu C. M., Lin Q., Wu T. X., Theoretical and Experimental Study on the Parametrically Excited Vibration of Mass-Loaded String, Journal of Nonlinear Dynamics, Vol. 37, pp 1-18, 2004.
- (6) Chen G., et al., Assessment of the Bill Emerson Memorial Cable-stayed Bridge Based on Seismic Instrumentation Data, Missouri Department of Transportation, Report No. OR08.003, September, 2007.
- (7) Hallquist J.O., LS-DYNA Keyword User's Manual, Livermore Software Technology Corporation (LSTC), Livermore, CA, 2009.
- (8) Dodds C. J., Robson J. D., The description of road surface roughness, International Journal of Sound and Vibration, Vol. 31, pp175-183, 1973.

- (9) Wang T. L., Huang D., Shahawy, M., Huang, K., Dynamic response of highway girder bridges, International Journal of Computers and Structures, Vol. 60, Issue 6, pp1021-1027, 1996.
- (10) Li H., Dynamic response of Highway Bridges Subjected to Heavy Vehicles, PhD Dissertation, Florida State University, Tallahassee, Florida, November, 2005.



### 3.3.4 Stability of Bridges with Piers in Scour Holes

Some of the work reported in this section was previously performed with USDOT/RITA funding. Subsequently, this research area became part of the current research sponsored by Turner Fairbank Highway Research Center. To introduce the work and maintain future continuity, both the earlier work and new work are included in this first quarterly report.

#### 3.3.4.1 Verify LS-DYNA multiphysics capabilities

In current design practice, soil-structure interaction analysis often assumes linear elastic properties of the soil and uses small displacement theory. However, there are numerous problems which require a more advanced approach. One such problem is the analysis of bridge pier stability under scour conditions where complex interactions occur between the bridge piers with footings and the surrounding soil. This type of problem requires special solution algorithms that account for soil-structure interaction and appropriate constitutive models for soil.

This study presents comparison of four numerical approaches to modeling soil-structure interaction in the presence of large soil deformations. The commercial code LS-DYNA®/MPP (1) was used to investigate the Lagrangian, Element Free Galerkin (EFG), Smoothed Particle Hydrodynamic (SPH) and Multi Material Arbitrary Lagrangian-Eulerian (MM-ALE) algorithms. To establish the accuracy and computational efficiency of each method, simulations were performed for the in-situ experiment of a steel loading pad penetrating into silty clay sand. The efficiency of the methods was assessed in terms of preprocessing complexity, robustness and computational cost. Solution accuracy was assessed by comparison to experimental results.

The results show that three of the four formulations can produce reasonable predictions at very large loading pad penetrations. However, the most reliable and efficient approach turned out to be the SPH method. This method was further used to investigate failure conditions of the pier of the Oat Ditch Bridge on I-15 in California during the August 2003 flood.

#### 3.3.4.1.1 Introduction

The Oat Ditch Bridge on I-15 in California (Bridge ID: 54-0270R) is a 5-span continuous reinforced concrete slab on 4 reinforced concrete bent columns (see Figure 3.3.11 a). Each column was supported by an individual rectangular footing as shown in Figure 3.3.11 b. Although analyzed for scour in 2000 and found to be not scour critical, three columns at bent five of the bridge failed during the flood on 08/19-20/2003. As reported by California DOT (2), during the flood the bending moment created by hydraulic forces caused the concrete failure at the juncture of the columns and the cap-beam in the pier bent. Additionally, the soil material around the pier must have been partially washed out and the support to the footing was weakened; this allowed for excessive displacement of the columns.

With the advancement of computational methods and the increase in computational power, engineers can use numerical methods for reconstruction of failure scenarios of events involving soil-structure interaction. The same techniques can be used to investigate the interaction of subsurface structures with the surrounding soil, especially when the structure is flexible and, thus, large deformations in the soil are likely to occur.

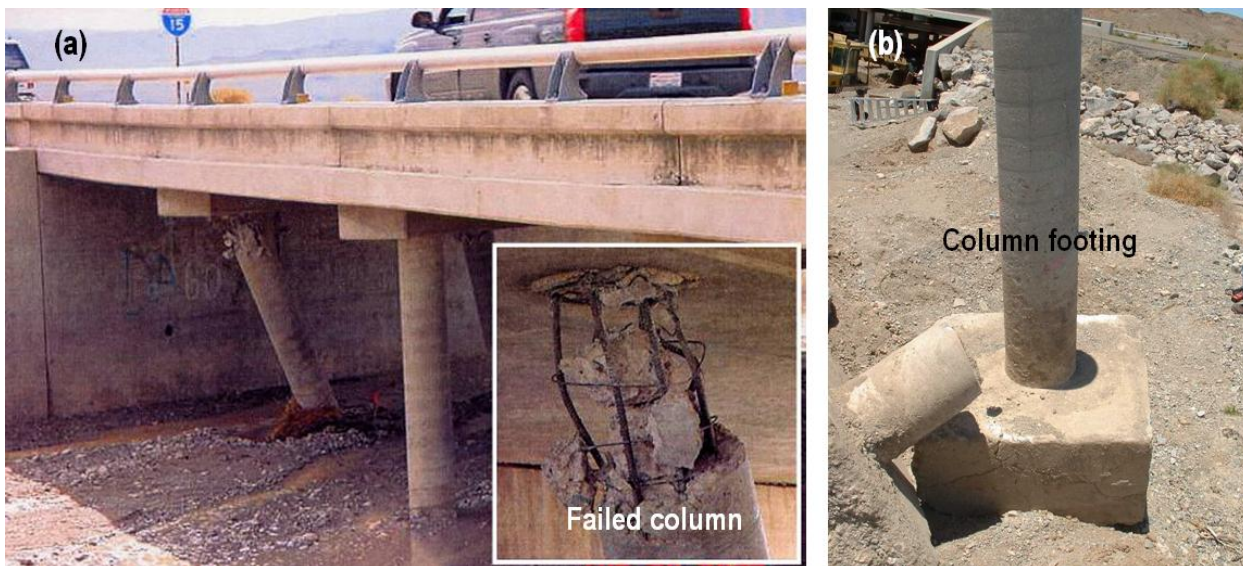


Figure 3.3.11: Oat Ditch Bridge on I-15 in California (a) failed column (b) column footing

This study compares four numerical methods for modeling large deformations in soil and soil-structure interaction using the LS-DYNA/MPP explicit code. The traditional Lagrangian Finite Element (FE) solution is compared to solutions from three relatively new methods: Element Free Galerkin (EFG), Smoothed Particle Hydrodynamic (SPH) and Multi Material Arbitrary Lagrangian - Eulerian (MM-ALE). The feasibility of the methods is examined on quasi static soil penetration test previously reported in (3) and (4). Subsequently failure conditions of the Oat Ditch Bridge are investigated. A numerical model of the bridge pier including surrounding soil was developed. The soil is represented by the most efficient method, i.e., FE combined with SPH, with estimated hydraulic forces acting on the column.

### 3.3.4.1.2 Simulation of Soil Penetration Test

The benchmark problem selected involves a previously reported quasi static soil penetration test (3); parts of our modeling approach also follow from (3). In the experiment, a 6 foot square by 5 foot deep test trench was filled with loose silty clay sand that was loaded using a 20 inch square steel plate. The displacement of the plate, the force exerted by it and the vertical stresses in the soil were recorded during the test.

The soil was modeled using the soil and crushable foam material model (LS-DYNA/MPP material MAT\_005). It is widely used in research areas like earth landing, roadside safety and others (5), (6), (7). This material model is very attractive to users because of the small number of material constants needed.

MAT\_005 uses a pressure dependent nonlinear Drucker-Prager yield function,  $\phi$ , that is described in terms of the second invariant,  $J_2$ , of the deviatoric stress tensor,  $s_{ij}$ , pressure,  $p$ , and constants  $a_0, a_1, a_2$  as:

$$\phi = J_2 - [a_0 + a_1 p + a_2 p^2] \quad (3.3.7)$$

Where:

$$J_2 = \frac{1}{2} s_{ij} s_{ij} \quad (3.3.8)$$

and the three constants are fit from laboratory triaxial test data points (3) using the relation:

$$\sigma_1 - \sigma_2 = \sqrt{3J_2} \quad (3.3.9)$$

**Table 3.5: Parameters used to define soil material using formulation MAT\_005 (units: mm-s-tonne)**

Parameter	Description	Value
RO	Mass density	1.440e-009
G	Shear modulus	34.474
K	Bulk modulus for unloading	15.024
a0	Yield function constant	0
a1	Yield function constant	0
a2	Yield function constant	0.602
PC	Pressure cutoff for tensile fracture (<0)	0
VCR	Volumetric crushing option	0 (on)
REF	Use reference geometry to initialize pressure	0 (off)
EPS1 ...	Volumetric strain values (natural log values)	see Figure 3.3.12
P1 ...	Pressures corresponding to volumetric strain	see Figure 3.3.12

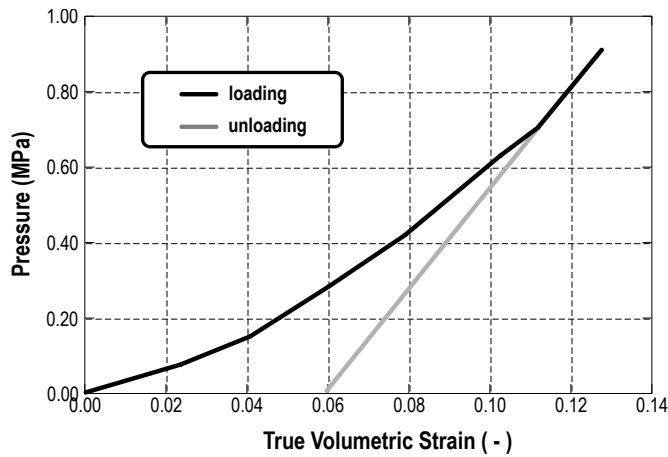


Figure 3.3.12: Triaxial hydrostatic compression data for soil material (3)

Table 3.5 contains the input parameters used to define the soil material for the comparison of methods and sensitivity studies. Figure 3.3.12 shows data from the triaxial hydrostatic compression test (pressure vs. true volumetric strain dependency).

A model of one quarter of the experiment was built with appropriate symmetry boundary conditions to represent the whole experiment. The soil model had side lengths of 2439 mm (96 in) and a depth of 1778.0 mm (70 in). On the outer and bottom faces, translational degrees of freedom were constrained. The square loading pad was modeled as a rigid material. A quarter of the Lagrangian model is shown in Figure 3.3.13 a. This model was used as a basis for models in other approaches.

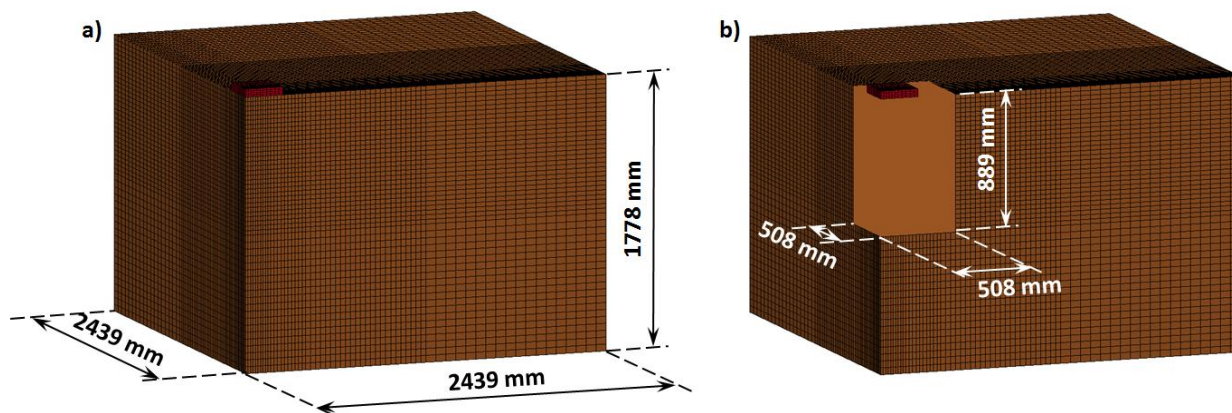
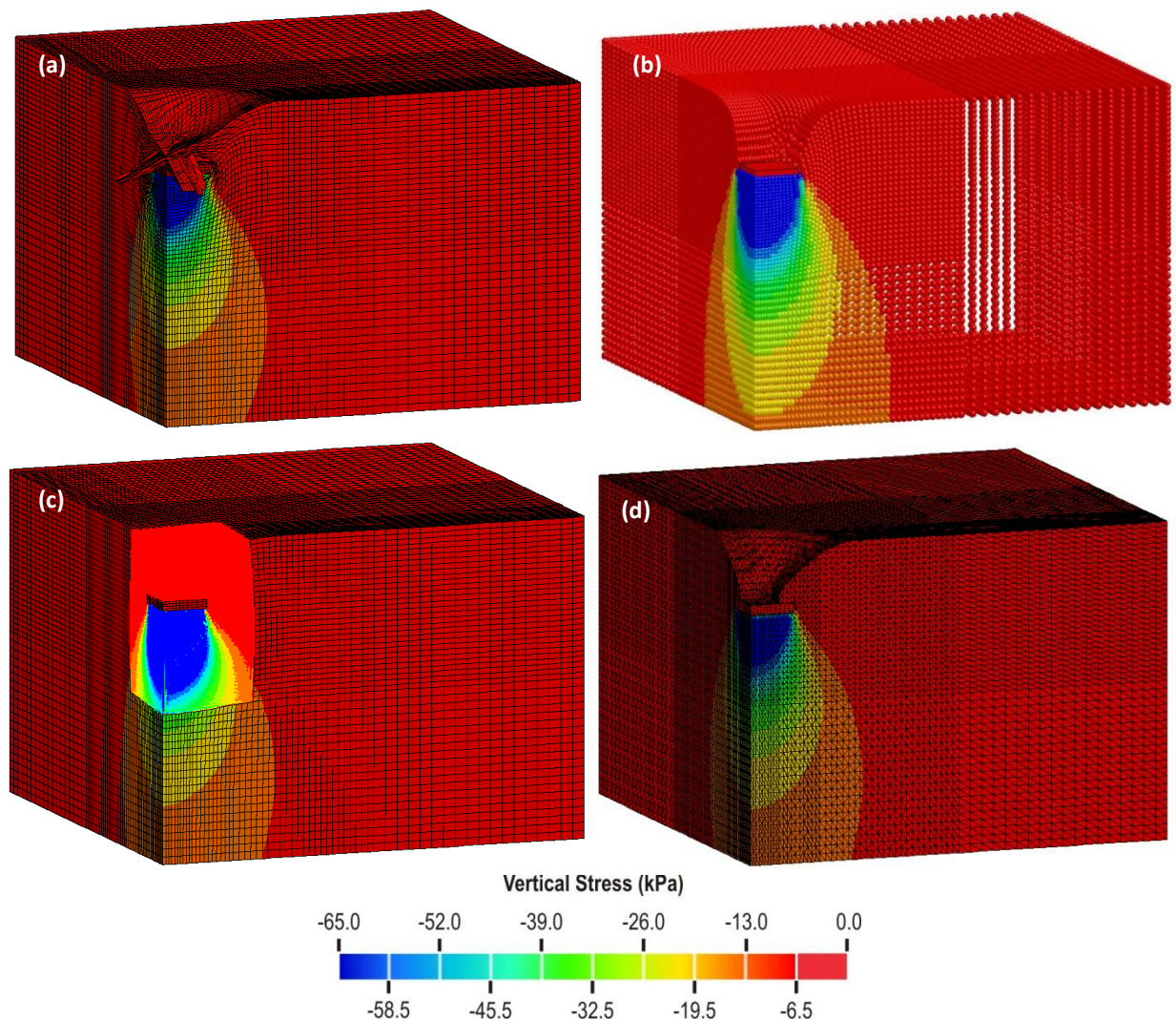


Figure 3.3.13: Numerical model for the soil penetration test simulation

In the combined Lagrangian-SPH model, the portion of the soil experiencing the largest deformations was modeled with SPH particles. The rest of the model was based on Lagrangian elements. The portion filled with SPH particles was 508 mm (20 inch) on each side and 889 mm (35 inch) deep. A quarter of the SPH model is shown in Figure 3.3.13 b.



The first 20 inches of load pad penetration into the soil was simulated. The loading pad was pressed into the soil with a constant rate of 1 in/sec. Figure 3.3.14 shows deformations predicted by each method at 15 inches of penetration. It is clearly visible that the Lagrange approach (i.e., traditional Finite Element method) fails to predict such large deformations. The mesh is highly distorted around the pad. All the other methods were able to capture the extremely large deformations.



**Figure 3.3.14: Deformations and vertical stresses at 15 inches of penetration:**  
 (a) Lagrange (b) EFG (c) SPH (d) MM-ALE

Figure 3.3.15 shows the force vs. loading pad penetration for each method. The Lagrangian method gave the softest response at large deformations. However, up to ~8 inches of penetration it was almost the same as the SPH and MM-ALE methods. The EFG method gave the stiffest response. It was discovered that changing the control parameters in the EFG analysis causes large changes in the response of the model. Thus, the EFG method should be used cautiously. The MM-ALE and SPH methods gave almost the same response. However, the SPH method turned out to be most robust.

The default settings were sufficient to run the simulation successfully. The MM-ALE required contact tuning to avoid spurious leakage of the material through the pad.

To assess the performance of the models, the results were compared with the experimental data reported by Schwer (3). The experiment consisted of pressing a loading pad into soil using a loading apparatus. However, because the apparatus was not capable of pressing the pad for the full 20 inches of penetration, it was sequentially started and stopped for the purpose of adding shim blocks that would allow deeper penetrations. This resulted in apparent load spikes during reloading (Figure 3.3.15 b) and potential deviation from a continuous loading curve. Also in the experiment, the force reading was zeroed at 1.27 inches of pad penetration. For comparison of the results, the simulation results were similarly adjusted by 1.27 inches. Experimental and simulation results are shown in Figure 3.3.15 b. The results for the four methods give good correlation with the experiment for the initial part of the curve. After the first drop in the experimental curve, they start to diverge – most likely due to the reloading step in the experiment. In particular, the large interval with zero load from 13.9 to 14.6 inches of penetration was noticeable and obviously could not occur in a continuous loading test. Also, there was only one test performed and, thus, the variation of results between multiple tests is unknown.

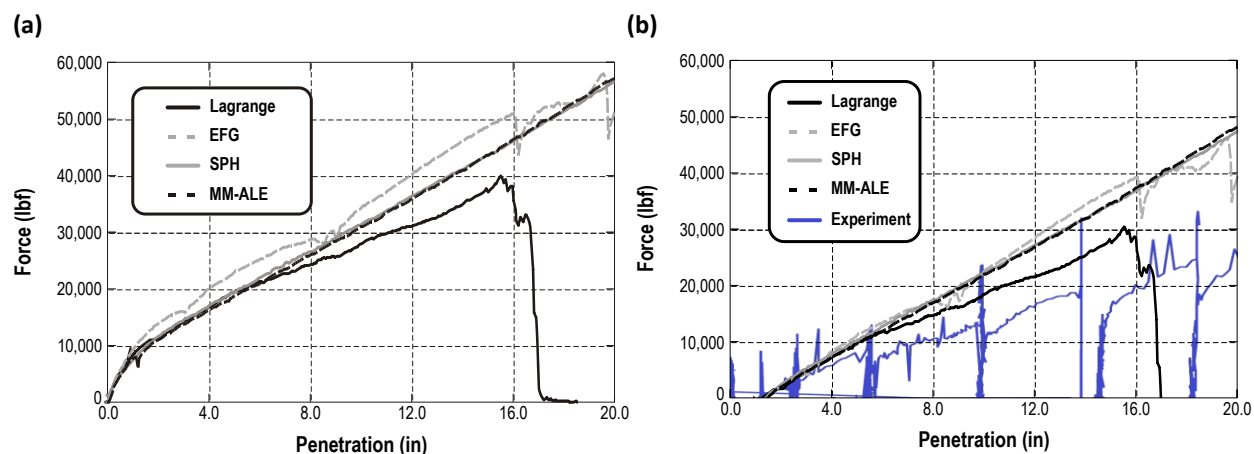


Figure 3.3.15: Simulation results for force as a function of loading pad penetration: Lagrange, EFG, SPH and MM-ALE (a) original results (b) comparison to experiment

### 3.3.4.1.3 Sensitivity Study

Quasi static loading is often hard to replicate in explicit simulations. For that reason penetration test simulations with different loading speeds were performed to evaluate the sensitivity of the model to strain rate. Each model was run with three rates  $V1 = 1$  in/sec,  $V2 = 5$  in/sec and  $V3 = 0.2$  in/sec. The results of these simulations are presented in Figure 3.3.16. For the Lagrangian model the material exhibited slight loading rate dependency. However, in the other models this phenomenon was not present. Thus, it was attributed to the distortions of the mesh (hourglass effect) in the vicinity of the pad. The most consistent results were obtained for SPH and MM-ALE models. Assumed loading rate was sufficient to simulate a quasi-static test.

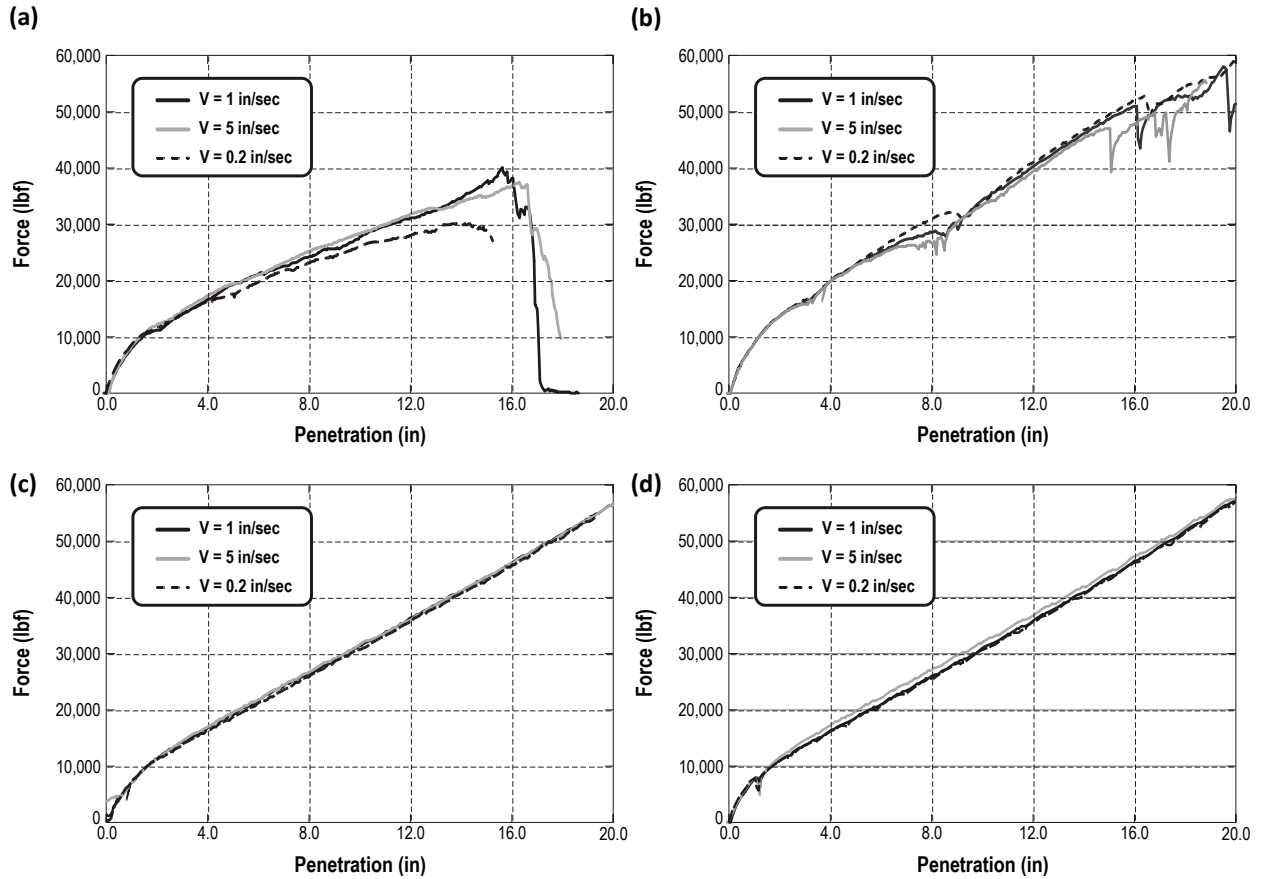
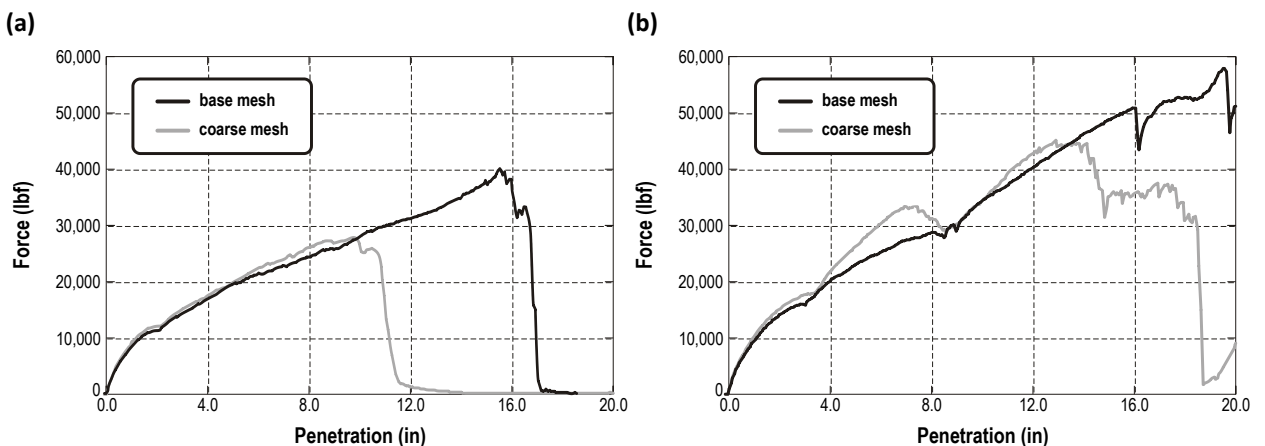


Figure 3.3.16: Effect of loading rate on force vs. penetration results:  
(a) Lagrangian (b) EFG (c) SPH (d) MM-ALE

An important factor for assessing the robustness of the solution is sensitivity to the change in mesh size. Here additional models with a coarse mesh were built. It turned out that the Lagrangian model failed to predict the results beyond 10 inches of penetration. Also, the EFG model did not give good results. Again the most stable and impervious to mesh size turned out to be the SPH model. The coarse mesh MM-ALE model shows slightly softer response.



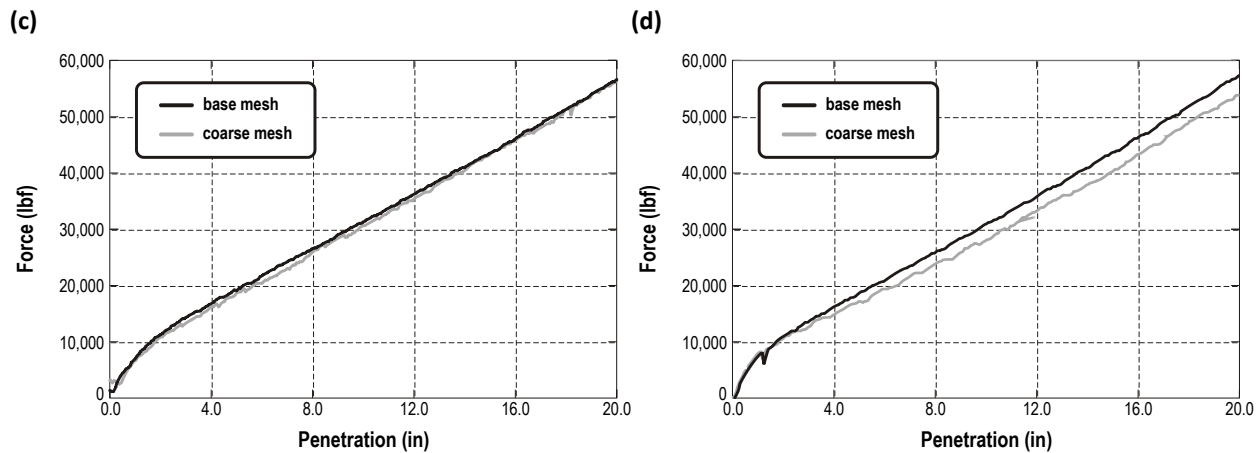


Figure 3.3.17: Effect of mesh size on force vs. penetration results  
(a) Lagrangian (b) EFG (c) SPH (d) MM-ALE

#### 3.3.4.1.4 Required Computational Resources

Each of the approaches analyzed have different demand on computational resources. To compare the computational demand of the methods, the initial 5 inches of penetration was simulated using each approach. All simulations for this portion of the study were run using single precision MPP-DYNA 971 revision 5.0 on 16 cores. Table 3.6 contains comparison of model size and the statistics on the running time for these models. The Lagrangian model took ~21.5 minutes. The MM-ALE model took 20.5 times longer than the Lagrangian simulation. The base SPH model took exactly 32 times longer. However, this model had two times more elements due to the recommendation that each face of the Lagrangian element should be in contact with at least four SPH nodes. Thus, another model with SPH particles was built that had a comparable number of elements to models from other methods. The simulation with the coarse SPH model took 5.3 times longer than the Lagrangian model. The EFG simulation turned out to be the fastest from the three non-standard approaches. It took about 2.5 times longer than the Lagrangian one.

Table 3.6: Simulation statistics at a penetration depth of 5 inches

	Lagrange	EFG	SPH	SPH coarse	MM-ALE
<b>No. of elements</b>	192,684	192,684	176,332 + 231,489 SPH particles	93,084 + 72,275 SPH particles	196,528
<b>Initial timestep</b>	6.93E-05	6.93E-05	6.92E-05	1.04E-04	6.85E-05
<b>Final timestep</b>	1.87E-05	6.45E-05	5.84E-05	7.71E-05	1.89E-05
<b>Total CPU time</b>	00 : 21 : 38	0 : 54 : 03	11 : 31 : 17	01 : 55 : 33	07 : 19 : 58



#### 3.3.4.1.5 Conclusions

Considering all these aspects, the SPH model with the coarse mesh turned out to be the best choice for predicting large deformations in soil. The SPH approach was insensitive to changes in loading rate and mesh size. The simulations were very stable and they did not require any parameter tuning to reach 20 inches of penetration. Thus, this method is recommended to be used for analysis of soil-structure interaction problems in the presence of large soil deformations.

In this study, large deformations in the soil were simulated using four formulations: Lagrangian, EFG, SPH and MM-ALE. Although the Lagrangian approach was the fastest and gave reasonably good results at moderate deformations, the mesh distortions disqualify this method for use in problems in which soil undergoes large deformations.

The EFG approach produced more reasonable soil deformations, but the soil had a stiffer response than in other methods. Also for the coarse mesh, contact problems occurred. The MM-ALE approach eliminated the problem of mesh distortion. However, the time spent on adjusting the contact parameters and the CPU time required for the simulation itself makes this approach less attractive.

The most robust and reliable approach turned out to be a hybrid approach that used the SPH formulation in the soil region with high material distortion and the Lagrangian formulation in the soil region away from the highly distorted part. The SPH approach was insensitive to loading rates. Also the CPU time required by this model was more favorable than by MM-ALE model. This method should be used in studies involving soil-structure interaction where the soil undergoes large deformations.

#### 3.3.4.1.6 Cone Penetration Test Simulations

During this quarter, a study on the standard cone penetration test (CPT) was also performed. The study was aiming to validate the selected previously approaches against the experimental data on the cone penetration tests. In this test friction between the soil and the cone surface plays a crucial role in providing the resistance force. The CPT procedure was based on ASAE Standard S313.2. The cone penetrometer had a  $30^\circ$  apex angle with a base area of  $323 \text{ mm}^2$  (radius of 10.14 mm). The penetrometer was modeled with shell elements and rigid type of material. All but vertical translational degrees of freedom of the cone were restrained. The full geometry of the cone was modeled. In the test, the cone penetrated the soil at a constant rate of 30.48 mm/sec (1.2 in/sec). 210 mm of penetration were simulated, which required approximately 7 seconds of simulation. Only a quarter of a cylindrical soil sample with radius 161 mm and depth of 400 mm was modeled. The soil model was constrained on the external, cylindrical side and on its bottom. Appropriate symmetry boundary conditions were applied on the internal faces. In the current study two approaches were used to model the soil: 1) hybrid between Lagrangian and SPH method and 2) Multi Material Arbitrary Lagrangian Eulerian method. Both models are presented in Figure 3.3.18.

In the hybrid Lagrangian-SPH model, a square core with width of 23.5 mm and depth of 267 mm was modeled with SPH particles. This assures that only SPH particles will be in the region where large

penetrations are expected. The Lagrangian elements in the rest of the model assure reasonable size of the model and computational efficiency. The hybrid model had in total 124,600 hexahedral solid and 90,000 SPH elements. The MM-ALE model had in total 192,500 hexahedral elements.

Also, two other previously used approaches (pure Lagrangian and Element Free Galerkin) were used in this study. However, the simulations were failing soon after the start. The sharp tip of the cone penetrating into the soil was causing contact problems and LS-DYNA was terminating the calculations with errors. Thus, these two approaches will be not described in this report.

The soil material was again modeled using LS-DYNA constitutive model MAT\_SOIL\_AND\_CRUSHABLE\_FOAM (MAT\_005). Two soil types were considered in the study: Norfolk sandy loam and Decatur clay. The material properties of the soil and results of CPT's were obtained from the study of W.A. Foster previously published in *Finite Element Simulation of Cone Penetration*, Pages 735-749, Vol. 162, Issue 2, International Journal of Applied Mathematics and Computation, March 2005. From the data presented, the True Volumetric Strain versus Pressure was obtained for each of the materials and are presented in Figure 3.3.19. The remaining material properties needed for MAT\_005 definition are listed in Table 3.7.

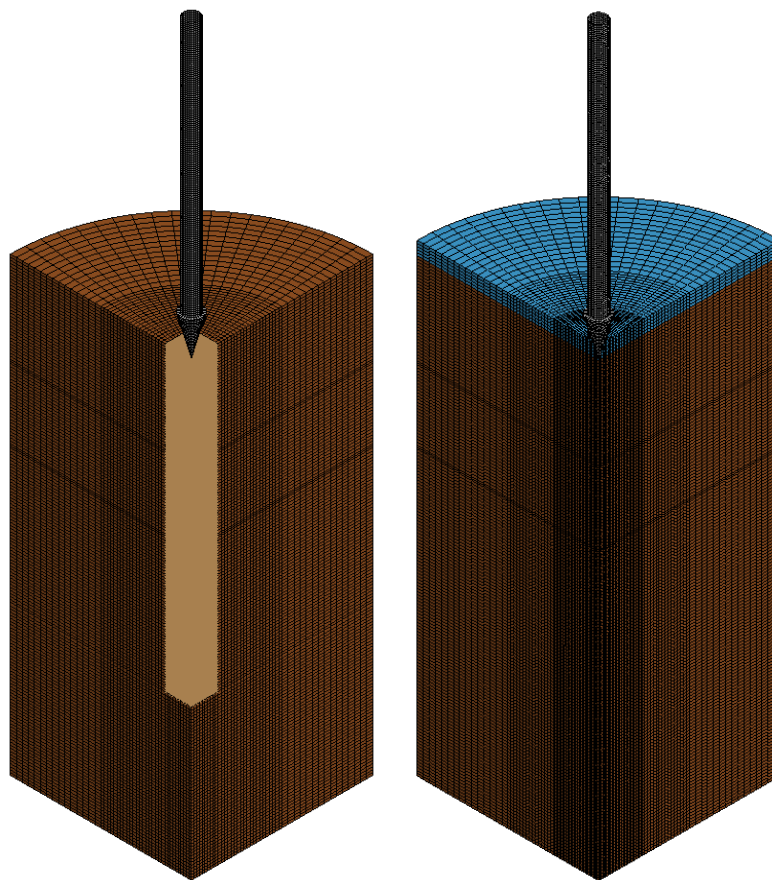


Figure 3.3.18: Numerical model for the cone penetration test simulation:  
(a) Hybrid Lagrangian-SPH model (b) MM-ALE model

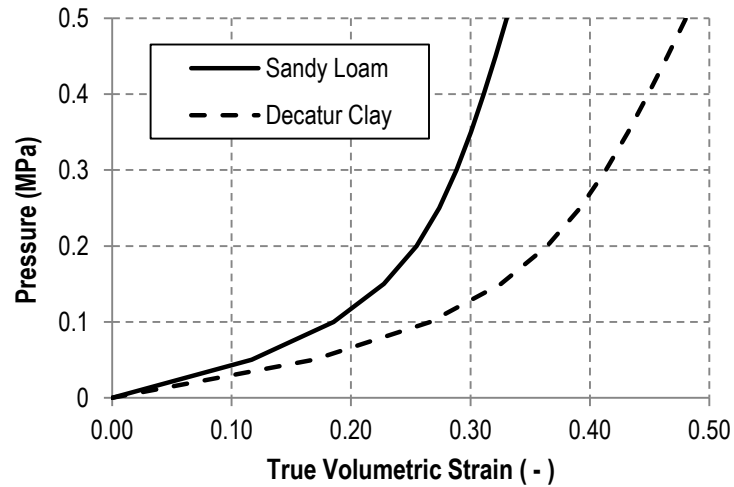


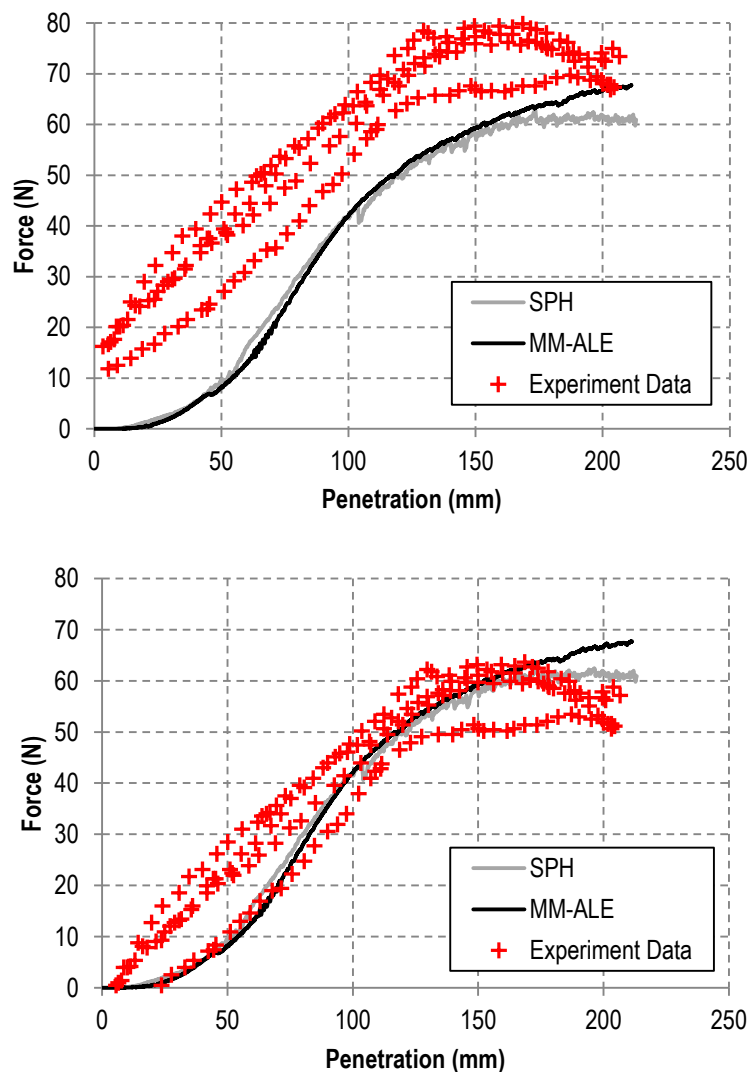
Figure 3.3.19: Triaxial hydrostatic compression data for soil materials

Table 3.7: Parameters used to define soil materials using formulation MAT\_005 (SI units: mm-second-tonne)

Parameter	Description	Norfolk Sandy Loam	Decatur Clay
RO	Mass density	1.2550e-009 t/mm <sup>3</sup>	1.0960e-009 t/mm <sup>3</sup>
G	Shear modulus	1.7240 MPa	1.7240 MPa
K	Bulk modulus for unloading	5.5160 MPa	5.5160 MPa
a0	Yield function constant	0	0
a1	Yield function constant	0	0
a2	Yield function constant	0.8702	2.2887
PC	Pressure cutoff for tensile fracture (<0)	0	0
VCR	Volumetric crushing option	0 (on)	0 (on)
REF	Use reference geometry to initialize pressure	0 (off)	0 (off)
EPS1 ...	Volumetric strain values (natural log values)	see Figure 3.3.19	see Figure 3.3.19
P1 ...	Pressures corresponding to volumetric strain	see Figure 3.3.19	see Figure 3.3.19

Figure 3.3.20 and Figure 3.3.21 show results from the numerical simulations. The curves show the dependency of soil vertical resistance force versus cone penetration depth. The registered response for the sand was very smooth. In contrast, the simulation for the clay material was noisy. The SPH and MM-ALE methods gave very similar responses for the sand. However in the final stage of loading, numerical problems occurred in the SPH simulation, and the soil resistance was weaker. In addition, experimental data (Foster et al.) was available for comparison to simulated results. Figure 3.3.20 a includes the data points from the reported experiments. In order to compare the experimental data with simulations' results, the experimental data points need to be shifted on the y-axis to the origin. This is due to initial slack in the testing apparatus. Figure 3.3.20b shows the translated data together with the numerical

results. The maximum resistance force and the character of the curve from the simulations match the experimental data very well.



**Figure 3.3.20: CPT data for Norfolk Sand**

The force – penetration curve for the clay material as obtained from LS-DYNA simulations was not smooth. Additionally, the response from the SPH method was much noisier than the response from MM-ALE method. This behavior is non-physical and is attributable to numerical problems with handling soft clay material. Figure 3.3.21 a shows the results from simulations together with the raw data from the experiments. Again the experimental data needed to be shifted down on the y-axis to the origin of the coordinate system. After this shift, the results from the simulations corresponded very well with the experimental data—only slightly underestimating the resistance force.

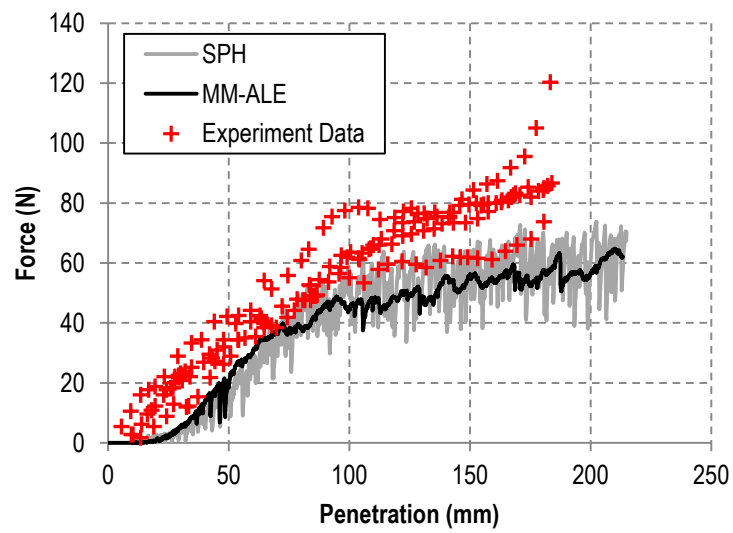
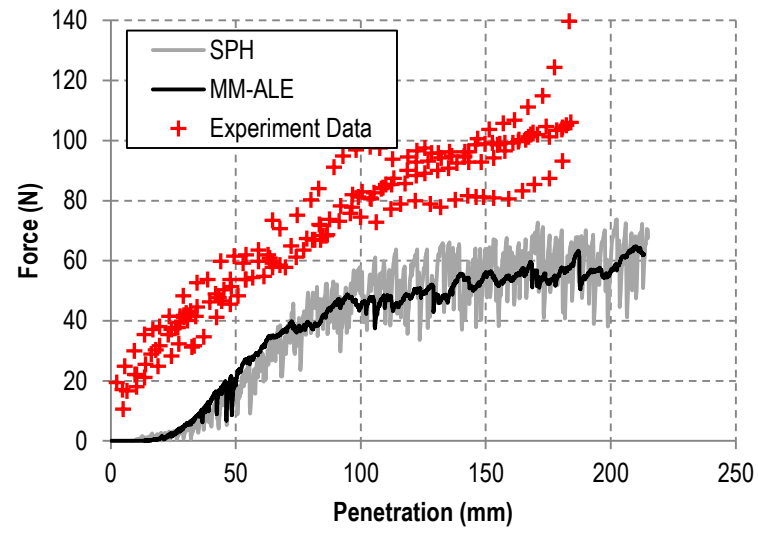


Figure 3.3.21: CPT data for Decatur Clay

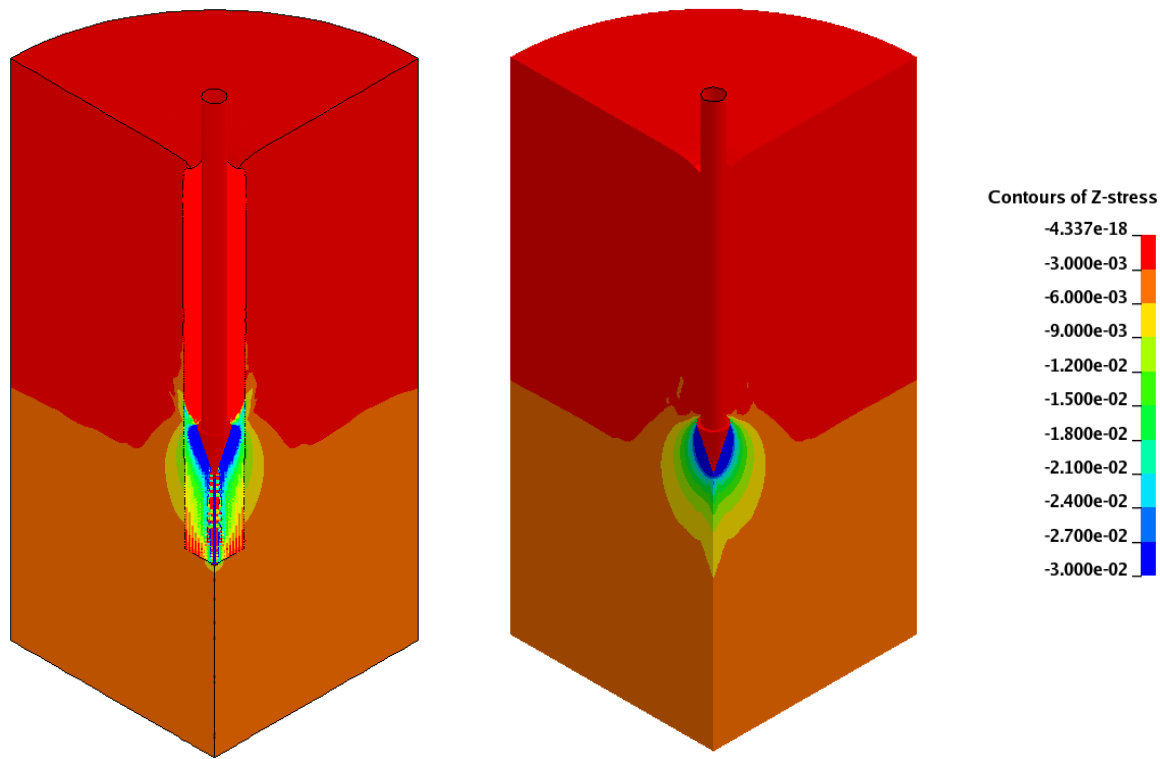


Figure 3.3.22: Deformations and vertical stresses at 210 mm of penetration:  
(a) SPH (b) MM-ALE

Figure 3.3.22 presents the vertical stresses in the soil from the hybrid SPH-Lagrangian (a), and the MM-ALE models (b). The distribution of stresses is much smoother in the MM-ALE method. Note, the SPH method produced non-uniform stresses in the vicinity of the loading point. This behavior was eliminated when a full cylindrical model was built.

As mentioned in the introduction, the resistance of the soil in a CPT test depends greatly on friction. Figure 3.3.23 shows the energy balance for the simulation of a CPT using the hybrid model. Approximately 35% of the total energy constitutes sliding energy, which in this case is energy due to friction. That indicates a possible sensitivity of the results to the friction coefficient between the cone and the soil.

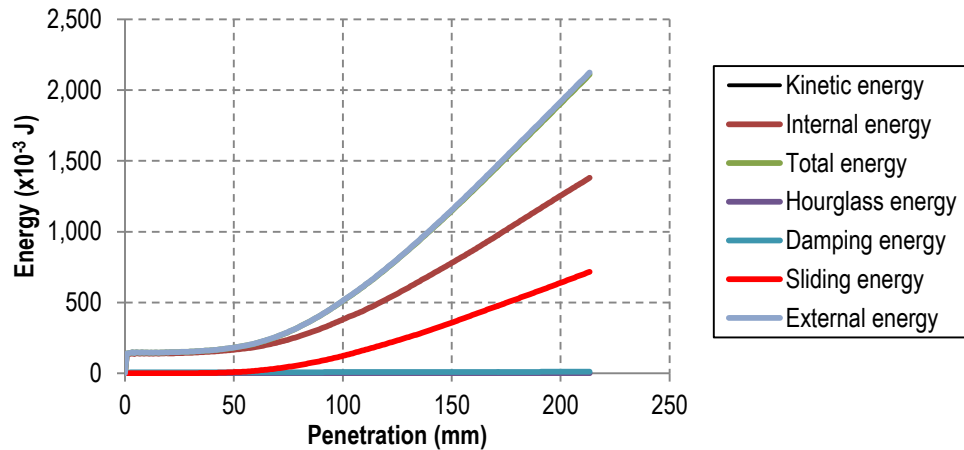


Figure 3.3.23: Energy Balance for CPT test simulation

A sensitivity analysis was performed with the LS-OPT software. Ten simulations were performed with the friction coefficient varying from 0.27 to 0.611. The vertical soil resistance forces for these cases are plotted in Figure 3.3.24. The maximum force varied from 59.8 N to 93.6 N. The results are highly sensitive to the changes in friction coefficient. Thus, appropriate caution needs to be applied when estimating the friction coefficient for the contact of the bridge pier with soil.

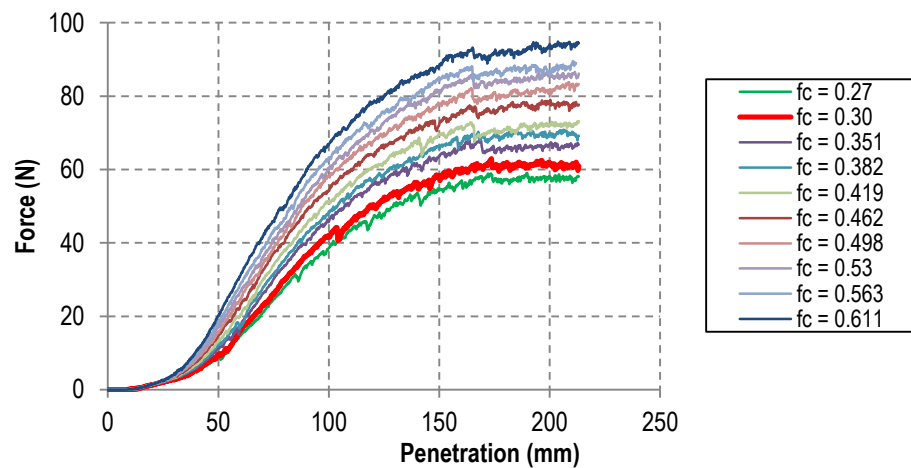


Figure 3.3.24: CPT simulations results for different friction coefficients between cone and soil

#### 3.3.4.1.7 References

- (1) Livermore Software Technology Corporation (LSTC), *LS-DYNA® Keyword User's Manual Version 971*, LSTC, 2007
- (2) California Department of Transportation (Caltrans), *Oat Ditch Bridge Failure, Internal presentation*, 2004

- (3) L. Schwer, *Soils and Foams Model Case Study*, Class notes: Concrete & Geomaterial Modeling with LS-DYNA, Schwer Engineering and Consulting Services, 2002
- (4) L. Schwer, *Laboratory Tests for Characterizing Geomaterials*, Class notes: Concrete & Geomaterial Modeling with LS-DYNA, Schwer Engineering and Consulting Services, 2001
- (5) E. L. Fasanella, R. K. H. Lyle, K. E. Jackson, *Developing Soil Models for Dynamic Impact Simulations*, NASA Langley Research Center
- (6) R. B. Timmers, R. C. Hardy, J.V. Welch, *Modeling and Simulation of the Second-Generation Orion Crew Module Air Bag Landing System*, NASA Langley Research Center
- (7) D. Marzougui, et al., *Evaluation of Rail Height Effects on the Safety Performance of W-Beam Barriers*, 6th European LS-DYNA Users' Conference, Gothenburg, Sweden May 29-30, 2007
- (8) Schwer L., Malvar L. J., *Simplified Concrete Modeling With \*MAT\_CONCRETE\_DAMAGE\_REL3*, JRI LS-DYNA User Week 2005, Nagoya, Japan, November, 2005
- (9) Abu-Odeh A., *Modeling Concrete Structures under Impact Loading: Applicability of Three Material Models*, TRB 2009 Annual Meeting, Washington D.C., 2009
- (10) Munson B. R., Young D. F., Okiishi T. H., *Fundamentals of Fluid Mechanics*, 5<sup>th</sup> Edition, John Wiley & Sons, Inc., 2006



### 3.3.4.2 Study effects of scour hole geometry and soil properties on pier stability

#### 3.3.4.2.1 Scour Hole Surface Representation for Structural Analysis

The topology of scour-holes is currently being investigated using three-dimensional CFD simulations. The resulting CFD topology would be site specific. For the purpose of rapidly performing scoping studies on the stability of bridge piers in scour-holes, a parametric representation of the scour-hole is needed for use in the computational structural mechanics code MPP-DYNA. This representation should be based on a few parameters that can provide a reasonable estimate of the surface topology of the scour-hole for the purpose of performing structural analysis: depth of the hole, width in flow direction, width across flow direction, and location of pier within the scour-hole. The initial approach, which was previously proposed by RFK Engineering Mechanics Consultants, was based on using a slanted elliptical paraboloid. With this approach, the distances from the scour-hole edge to the center of the pier in the upstream and downstream directions were controlled by the angle of the slant. This approach was satisfactory but did not lend itself to doing parameter studies because the depth was hard to determine *a priori*.

The following describes a recent modification to the original approach for embedding the surface of a scour-hole into soil around a bridge pier for studying bridge stability. In the original approach, the elliptic paraboloid of height  $h$ , semimajor axis  $a$ , and semiminor axis  $b$ , was specified parametrically by:

$$\begin{aligned}x &= a\sqrt{u} \cos v \\y &= b\sqrt{u} \sin v \\z &= u\end{aligned}\tag{3.3.10}$$

For  $v \in (0, 2\pi)$  and  $u \in (0, h)$

With the original approach, to get different upstream and downstream shapes, the elliptic paraboloid is tilted. The following approach is easily adaptable to doing this type of parameter study. The modified approach considers a vertical elliptic paraboloid, but the major and minor axes,  $a$  and  $b$ , are allowed to vary as follows:

For  $v \in (0, \pi)$

$$\begin{aligned}a &= A\left(1 + n\frac{v}{\pi}\right) \\b &= B\left(1 + m\frac{v}{\pi}\right)\end{aligned}\tag{3.3.11}$$

For  $v \in (\pi, 2\pi)$

$$\begin{aligned}a &= A\left[1 + n\left(2 - \frac{v}{\pi}\right)\right] \\b &= B\left[1 + m\left(2 - \frac{v}{\pi}\right)\right]\end{aligned}\tag{3.3.12}$$

Where “A” and “B” are the initial values for the semi-major axes, and  $n$  and  $m$  are scale factors use to control the upstream and downstream sizes of the scour-hole. Having separate scale factors allows for independent control of each semi-major axis. Note, Equations (2) and (3) each apply to one-half of the scour-hole.

It has been determined that using Equations (2) and (3) can produce reentrant surfaces that lead to cusps at  $\nu = 0$  and  $\nu = \Pi$ , which would be non-physical. Regularization of the scale factor will be used to eliminate this. The regularization,  $R_c(\nu)$ , chosen is given by:

$$\begin{aligned} R_c(\nu) &= \frac{\nu}{\nu_c}, \text{ if } \nu < \nu_c \\ R_c(\nu) &= 1, \text{ if } \nu > \nu_c \end{aligned} \quad (3.3.13)$$

Where  $\nu_c$  is the cut-off angle. The above regularization is a ramp function, which varies linearly from 0 to 1, up to the cutoff angle and then has a constant value of 1.

Adding the regularization into Equations (2) and (3) gives

For  $\nu \in (0, \pi)$

$$\begin{aligned} a &= A(1 + R_c(\nu)n\frac{\nu}{\Pi}) \\ b &= B(1 + R_c(\nu)m\frac{\nu}{\Pi}) \end{aligned} \quad (3.3.14)$$

For  $\nu \in (\pi, 2\pi)$

$$\begin{aligned} a &= A[1 + R_c(\nu)n(2 - \frac{\nu}{\Pi})] \\ b &= B[1 + R_c(\nu)m(2 - \frac{\nu}{\Pi})] \end{aligned} \quad (3.3.15)$$

It was numerically determined that  $\nu_c = \frac{\pi}{4}$  gives a smooth transition between the regularized and non-regularized parts. An example of a regularized elliptical paraboloid (REP) is shown in Figure 3.3.25.

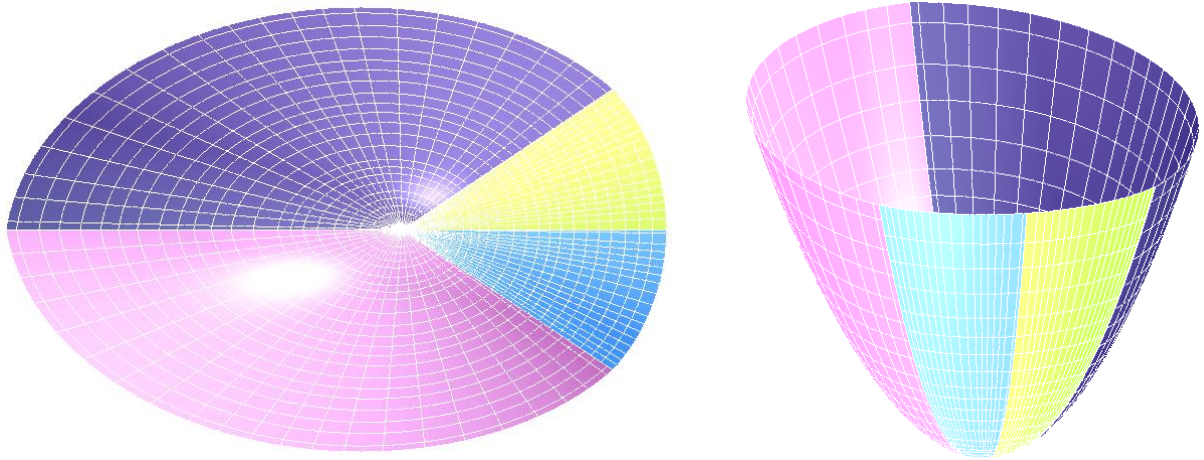


Figure 3.3.25: Elliptic paraboloid for representing the surface of a scour-hole: top view on left; perspective view on right

Since scour-hole depth would be a known, having the axis vertical is an advantage for exactly matching scour-hole depth. The differences in upstream and downstream shape are taken care of by the variable semi-major axes.

The vertex of the REP should be placed at the nose of the pier on the upstream side at the desired scour-hole depth. It is anticipated that the larger semi-major axis would lie in the direction of flow.

### 3.3.4.3 Analyze stability of existing bridges

#### Simulation of Oat Ditch Bridge Pier Failure

The Oat Ditch Bridge on I-15 in California (Bridge ID: 54-0270R) is a 5-span continuous reinforced concrete slab on 4 reinforced concrete bent columns (see Figure 3.3.26 a). Each column was supported by an individual rectangular footing as shown in Figure 3.3.26 b. Although analyzed for scour in 2000 and found to be not scour critical, three columns at bent five of the bridge failed during the flood on 08/19-20/2003. As reported by the California DOT, during the flood the bending moment created by hydraulic forces caused the concrete failure at the juncture of the columns and the cap-beam in the pier bent. Additionally, the soil material around the pier must have been partially washed out and the support to the footing was weakened; this allowed for excessive displacement of the columns.

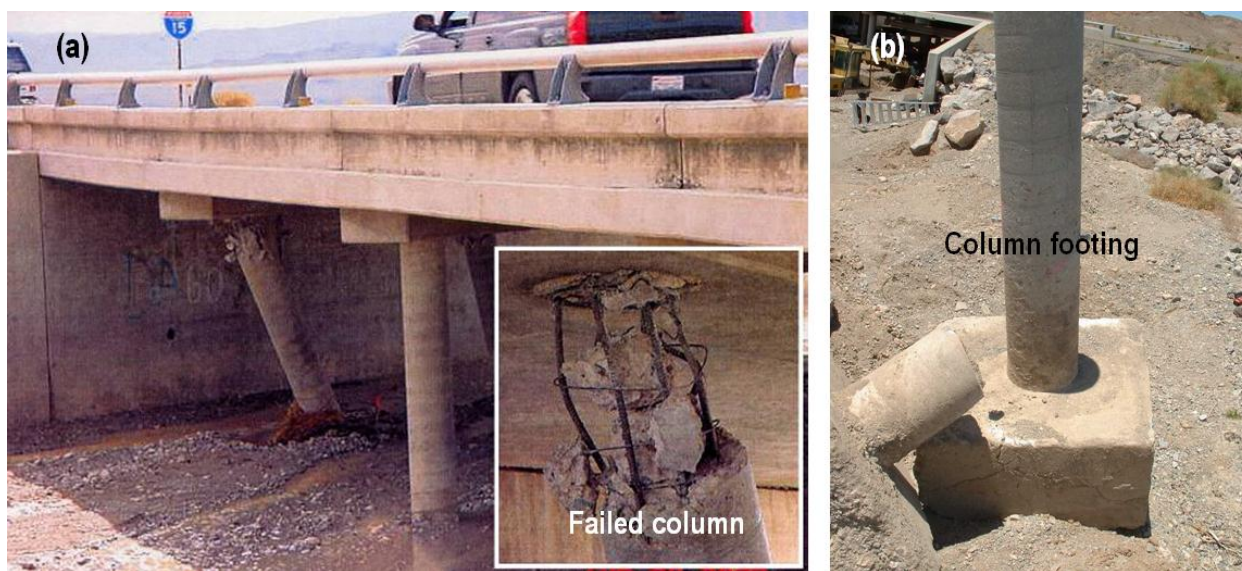


Figure 3.3.26: Oat Ditch Bridge on I-15 in California (a) failed column (b) column footing

Based on as-built drawings, a FE model of the Oat Ditch Bridge was developed for comprehensive study. In the current analysis, only one column of bent 5 was considered. The FE model included a portion of the bent cap, the column, the footing and the soil around it as shown in Figure 3.3.27. The soil was modeled using the Lagrangian-SPH approach previously described. For this initial study, the shape of the scour hole was considered to be flat in the region around the pier footing.

The concrete material was modeled with LS-DYNA material MAT\_072. MAT\_072 allows for modeling complex concrete behavior, including damage and failure, even with input limited to the unconfined compressive strength and density of the concrete. The non-linear response of the concrete is approximated from empirical data gathered in the MAT\_072 definition within LS-DYNA. The strength of the concrete was taken to be 27.58 MPa (4000 psi), and its density was taken to be  $2.320 \times 10^{-9} \text{ kg/m}^3$ . The steel rebars were modeled using beam elements with the default Hughes-Liu element formulation. Piecewise linear plasticity material model (MAT\_024) was used to model structural steel with Young's modulus of 205 GPa and yield strength of 298 MPa. The reinforcement was embedded in the concrete

using the `CONSTRAINED_LAGRANGE_IN_SOLID` keyword in LS-DYNA. This method does not require beam nodes to coincide with concrete solid elements. Fully constrained boundary conditions were assumed at the top of the pier bent.

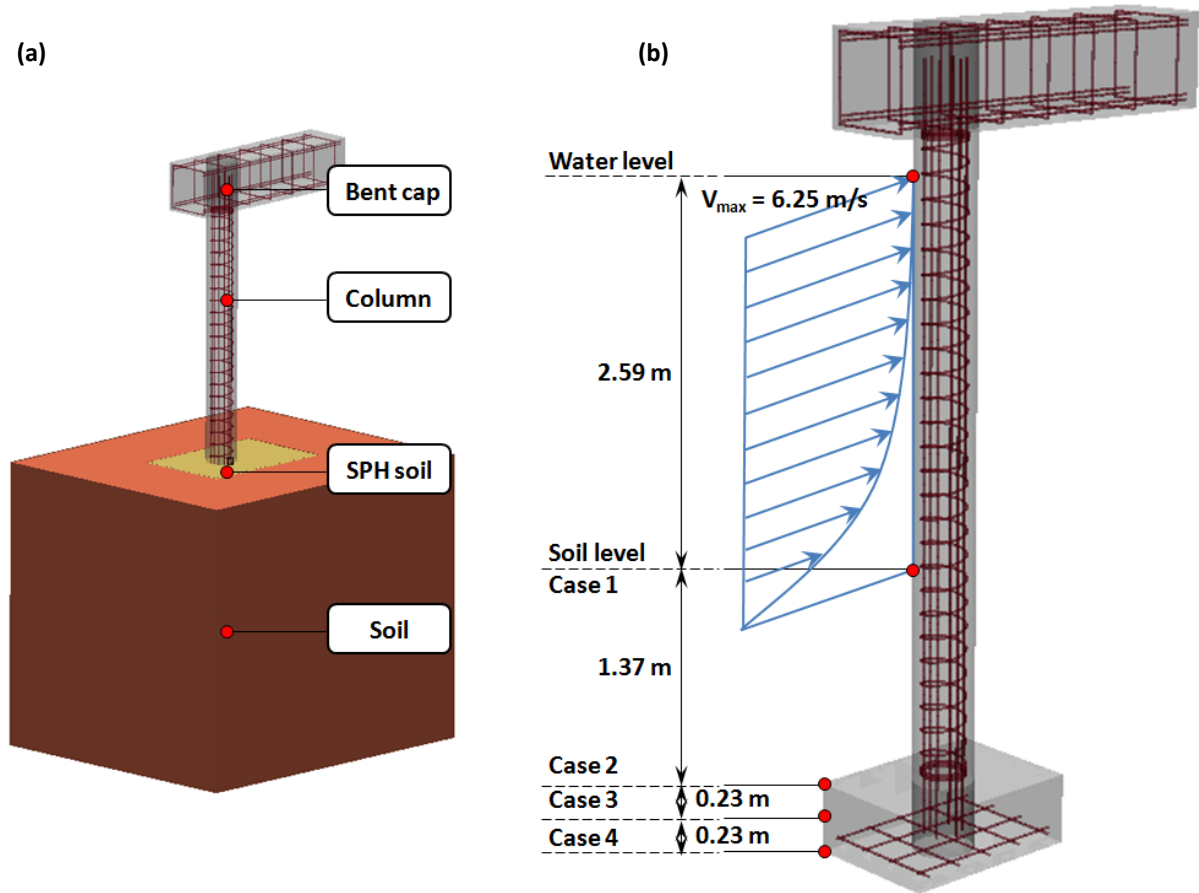


Figure 3.3.27: Computational model of the bent cap, column and soil of the Oat Ditch Bridge

An examination of the soil after the flood showed that loose sand was above the footing and that poorly graded, very dense, fine sand (SP) with a trace of silty fines was below the footing. Since no soil tests were performed and there was some similarity with the description of the soil used in the previous steel plate penetration test, the available properties were used.

Four loading cases were analyzed with different levels of water and soil. In Case 1, the level of the soil was modeled at the reported height after the flood. As shown in Figure 3.3.27, it was around 1.37 m above the footing's top surface. Since analysis of this case did not show failure of the column, other loading conditions were analyzed to find the critical level of the soil. In Case 2, the soil was taken to be at the top surface of the footing. In Case 3, the soil was taken to be at half of the footing height, and in Case 4 the soil is beneath base of the footing. No data was available for the shape, widths or depth of the scour hole. For this initial analysis, a flat scour hole (FSH) profile was assumed in the vicinity of the pier. It is conservative in the sense that for this profile the riverbed soil would provide the least resistance to pier-footing movement.

The drag force acting on the column due to the flowing water can be estimated from the equation:

$$F_d = \frac{1}{2} \rho u^2 C_D A \quad (3.3.16)$$

Where:

- $\rho$  – mass density of the fluid
- $u$  – velocity of the fluid
- $C_D$  – drag coefficient
- $A$  – reference area

To determine the drag coefficient,  $C_D$ , the Reynolds number needs to be calculated from:

$$R_e = \frac{uD}{\nu} \quad (3.3.17)$$

Where:

- $D$  – diameter of column
- $\nu$  – kinematic viscosity coefficient

It was reported that the maximum velocity of the water during the flood was 6.25 m/s (20.5 ft/s) and the average velocity was around 5.334 m/s (17.5 ft/s). The Reynolds number can be calculated from:

$$R_e = \frac{5.334 \text{ m/s} \cdot 0.3937 \text{ m}}{1.307 \text{ m}^2/\text{s} \cdot 10^{-6}} = 1,606,730 \quad (3.3.18)$$

From the graph of  $R_e - C_D$ , it is safe to assume that  $C_D = 1$ . Then the drag force and average pressure for the reported soil level can be estimated as:

$$F_d = \frac{1}{2} \cdot 1400 \text{ kg/m}^3 \cdot (5.334 \text{ m/s})^2 \cdot 1 \cdot 0.3937 \text{ m} \cdot 2.59 \text{ m} = 20.308 \text{ kN} \quad (3.3.19)$$

$$p_d = 20.308 \text{ kN} / 1.020 \text{ m}^2 = 0.01992 \text{ MPa} \quad (3.3.20)$$

Where  $\rho$  was assumed to be  $1400 \text{ kg/m}^3$  for water with 15% of sediment.

In a similar way, the drag force for other cases of soil level was estimated. The hydraulic load was applied to the external surface of the column as a non-uniform pressure. The pressure was ramped up from zero to the maximum level in 0.5 sec, and then the load was kept constant. For each case, the simulation time was 1 second.

For the four cases, Figure 3.3.28 shows the displacements of the footing as a function of time. For the Case 1, the displacement of the footing was barely noticeable. When the soil level was modeled only up to the top surface of the footing (Case 2), the displacement of the footing reached ~21 mm.

With the soil level modeled up to the half of the footing height (Case 3), cracking of the concrete at the bent occurred. Note, the material model considers the concrete initially to be crack free. The first concrete elements started to crack at ~0.67 sec of simulation or ~142 mm of displacement of the footing. For the case without the soil (Case 4), the first crack occurred at ~0.27 sec, which was equivalent to ~192 mm of footing horizontal displacement.

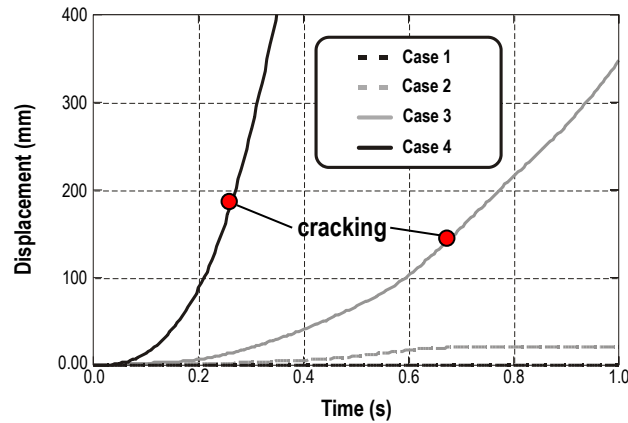


Figure 3.3.28: Displacement of the footing as a function of time

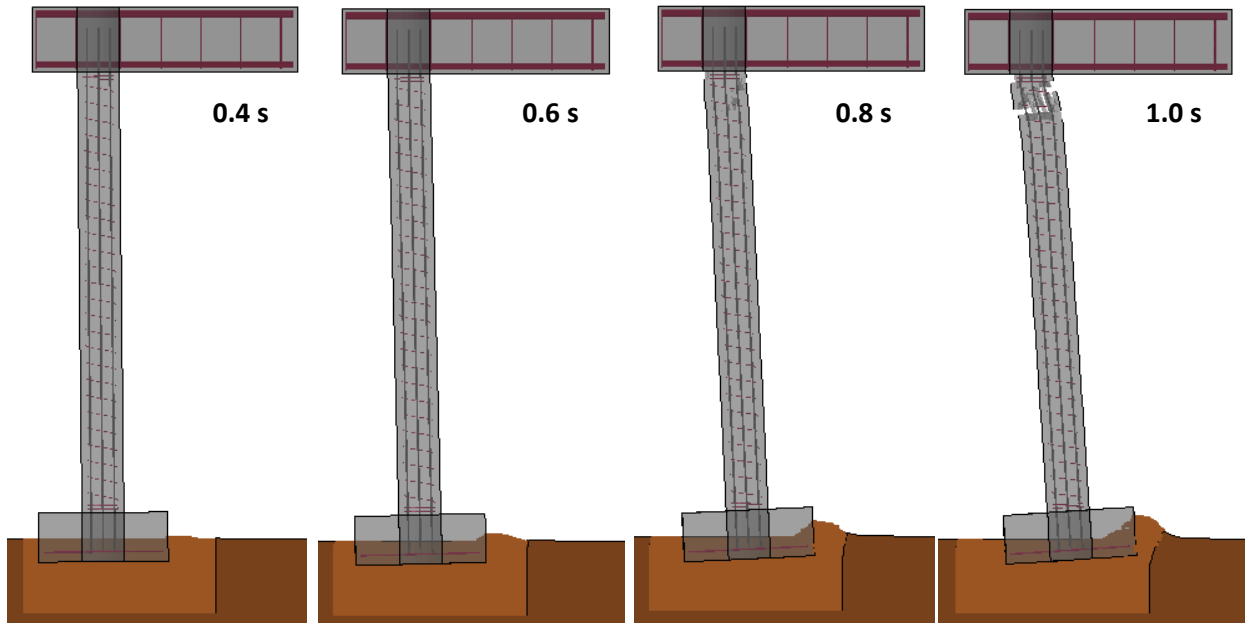


Figure 3.3.29: Deformation in the soil and the column for Case 3

Figure 3.3.29 shows deformations in the column during the simulation of loading Case 3. Large deformations in the soil around the footing and failure of the column can be seen. It is seen that the extremely large deformations occur in the SPH part of the model and large but not as severe deformations occur in the surrounding Lagrangian part of the soil model. A check on element distortion metrics for the soil represented in the Lagrangian domain show that they are well within the Lagrangian's formulation capability. Since both parts of the model use the same constitutive model for the soil, the transition between them is smooth and there is no confinement effect from the Lagrangian



part. From the cases analyzed, it can be concluded that during the flood the soil must have been washed out to largely uncover the footing. In the case when the soil was above the top of the footing the displacements were small and no failure in the column occurred.

The REP was used to create a scour hole in the riverbed soil for studying stability of the Oat Ditch Bridge. The previously developed FE structural model of the Oat Ditch Bridge was used in this study. Also, the above scheme for applying hydraulic pressure from the flood water to the column was used here. The only difference between the two studies is the scour-hole shape. In the previous study, the scour hole was considered to be flat, and in this study the shape is a regularized elliptical paraboloid. It is intended to use this procedure when basic data on scour-hole dimensions from the field measurements are known or for performing parameter studies. Here several cases with varying scour-hole depths were analyzed. The bottom face of the footing was taken to be 657 mm under the non-scour soil surface. In the cases studied, the scour hole had depths of 500 mm, 600mm and 700 mm (as measured from the riverbed surface to the apex of the REP). Thus, in all three cases, the footing was partially uncovered. The shape of the scour hole was generated using the Truegrid® mesh generator. The SPH particles filling the space occupied by soil in the model was generated using LS-PREPOST software. Figure 3.3.30 shows a cross section through the model with a 500 mm deep scour hole—as measured from the riverbed surface to the apex of the REP. It can be seen that the upstream edge of the hole is much closer to the pier than the downstream edge. The soil next to the upstream side of the footing is above the top surface of the footing, and the soil next to the downstream side is at the top of the footing.

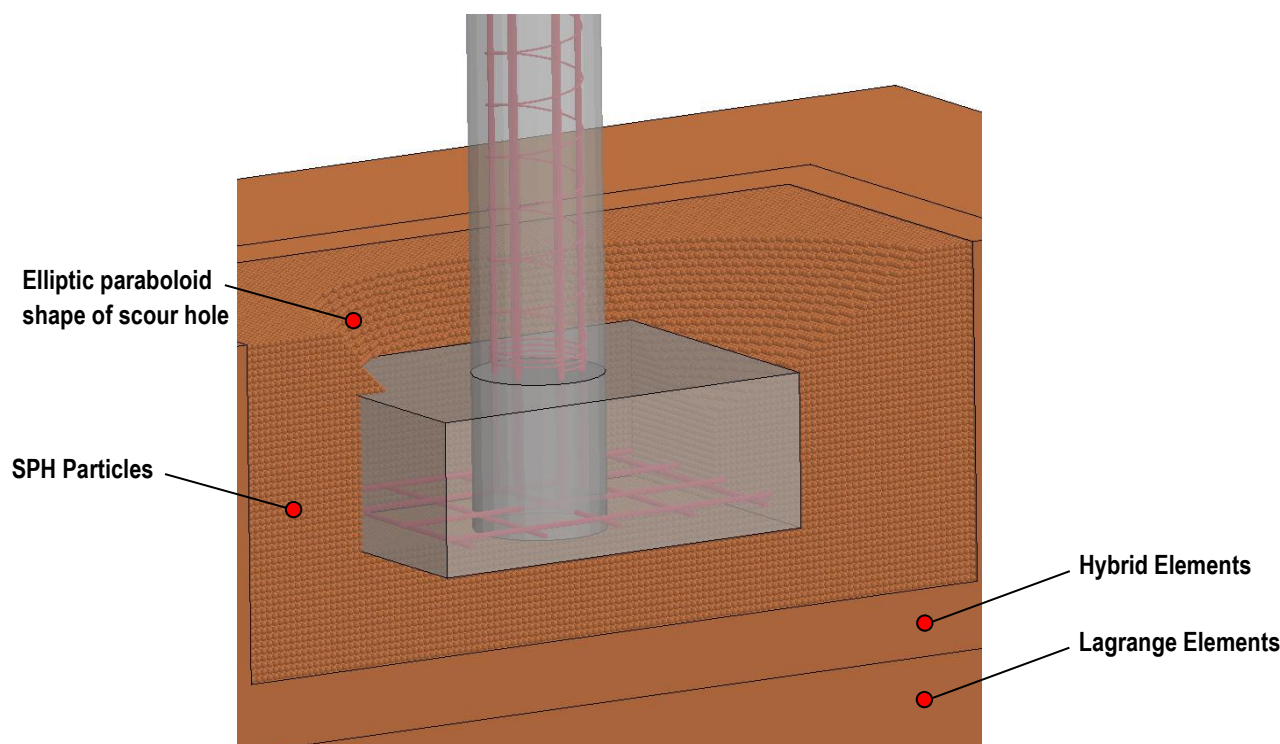


Figure 3.3.30: Bridge pier with footing embedded in a scour-hole represented by a regularized elliptical paraboloid

As in the cases with the flat scour hole profile, the lateral displacement of the footing was obtained from the simulations. In all cases analyzed, the displacement was very small. For the case with a 700 mm deep



scour hole (i.e., 80 mm of soil covering the downstream side of the footing), the footing moved about 40 mm (see Figure 3.3.31). It should be noted that unlike the FSH profile, the REP profile has soil with decreasing depth (i.e., increasing height) on both the upstream and downstream sides of the scour hole. Thus, for the case where the scour hole is at the bottom of the footing on the downstream side, the depth of the scour hole decreases in the downstream direction (i.e., more soil in the vertical direction), and the soil provides resistance to movement. This shows the importance of the soil on the downstream side of the footing in maintaining pier stability and, thus, preventing eventual collapse of the bridge.

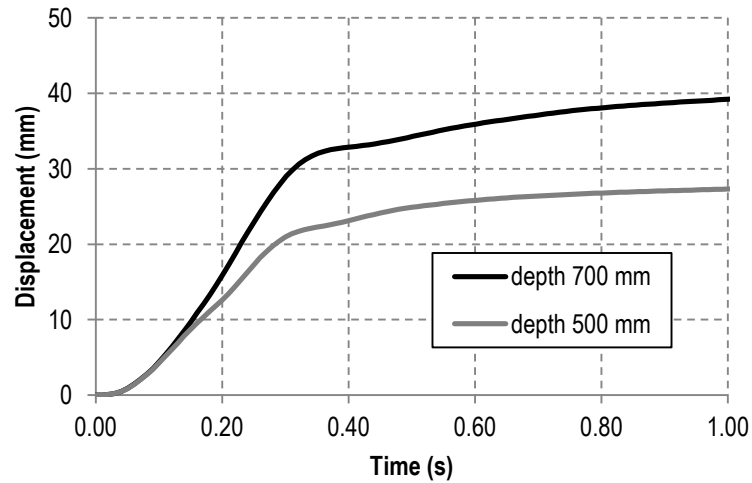


Figure 3.3.31: Displacement of the footing as a function of time

### 3.3.5 Modeling of Salt-Spray Transport Beneath Steel Bridges

#### 3.3.5.1 Using LS-DYNA Capabilities to model truck – spray interaction

##### 3.3.5.1.1 Introduction

In the 1970's, the use of weathering grade steel became popular in the fabrication of steel bridges in the US. The unique alloying with copper and nickel allowed the steel to develop a hard rust patina that did not flake off like conventional rust. This characteristic of weathering steel offered reduced fabrication and maintenance because coating the steel was no longer required. However, some states in the 1980's experienced greatly accelerated corrosion of weathering steel bridges. Depending on the geometry and aerodynamics of the bridge/tunnel system, salt-spray dispersed by vehicles driving over wet roads could be transported to the overhead steel girders. Once the chloride depositions become dense enough, corrosion of weathering steel becomes accelerated, exacerbated by the continuously moist conditions. In 1989 the Federal Highway Administration (FHWA) issued Technical Advisory 5140.22 to warn bridge owners of situations where weathering steel should not be used.

The Turner Fairbank Highway Research Center (TFHRC) currently is interested in studying the transport of salt spray generated by vehicle tires from the pavement up to the exposed steel support beams of steel bridges as the tires roll over wet pavement (Figure 3.3.32). The research is aimed to update the Technical Advisory, which is already over 20 years old, with results based on current state-of-the-art computational analysis and experimental data acquired at critical locations.

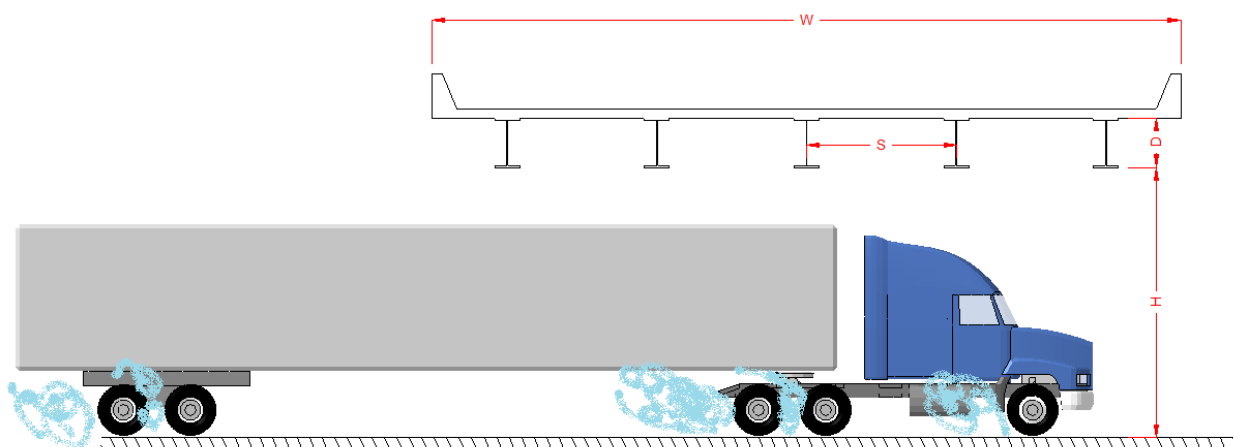


Figure 3.3.32: Semitrailer traveling through a bridge underpass

##### 3.3.5.1.2 Modeling Approach

A modeling approach has been proposed by RFK Engineering Mechanics Consultants that uses the multi-physics capability of the LS-DYNA® software. Specifically, the multi-material Arbitrary Lagrangian Eulerian (MM-ALE) formulation will be used. Initially, a feasibility study will be performed to determine the computational characteristics of the problem and to see if the MM-ALE approach is tractable. The problem will consist of a semi-trailer truck traveling through a bridge underpass. The truck will be

treated as a rigid body defined by a finite element mesh. The underpass will be represented by a stationary (i.e., fixed in space) Eulerian mesh containing air. A finite element model of a semitrailer truck and a rectangular MM-ALE domain containing air was developed. For the feasibility study and the sake of simplicity, the top of the MM-ALE domain was flat and represented the bottom of the bridge—bridge support beam details were not included. More sophisticated models will be developed later in the project that includes the topology of the underside of the bridge.

The model of a truck tractor was based on the Mack CH 613 tractor. The spacing of the axels are shown in Figure 3.3.33 a. The sleeper and the dry freight van type trailer were also modeled (see Figure 3.3.33 b). The biggest allowed - 16.16 m long and 2.89 m wide - trailer was modeled as shown in Figure 3.3.34. The entire semi-trailer truck model was built as one LS-DYNA part with the material specified as rigid to represent a rigid body. In the next quarter, a study will be performed on truck interaction with the salt spray clouds.

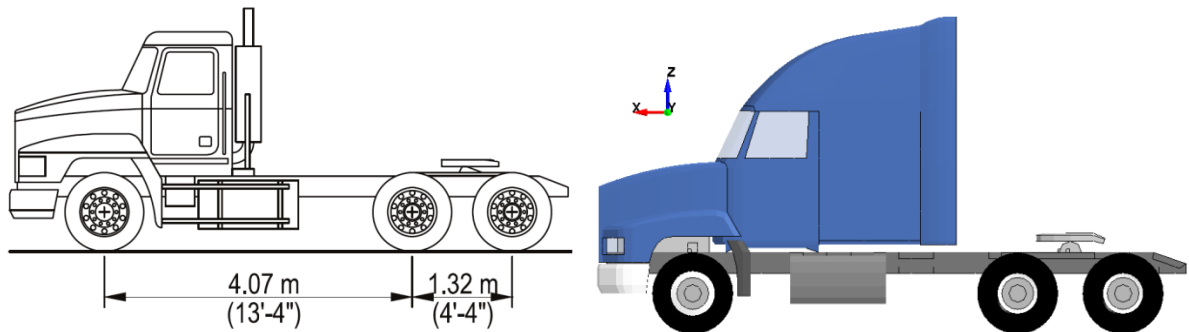


Figure 3.3.33: Mack CH 613 tractor (a) schematics (b) FE model of the tractor with a sleeper

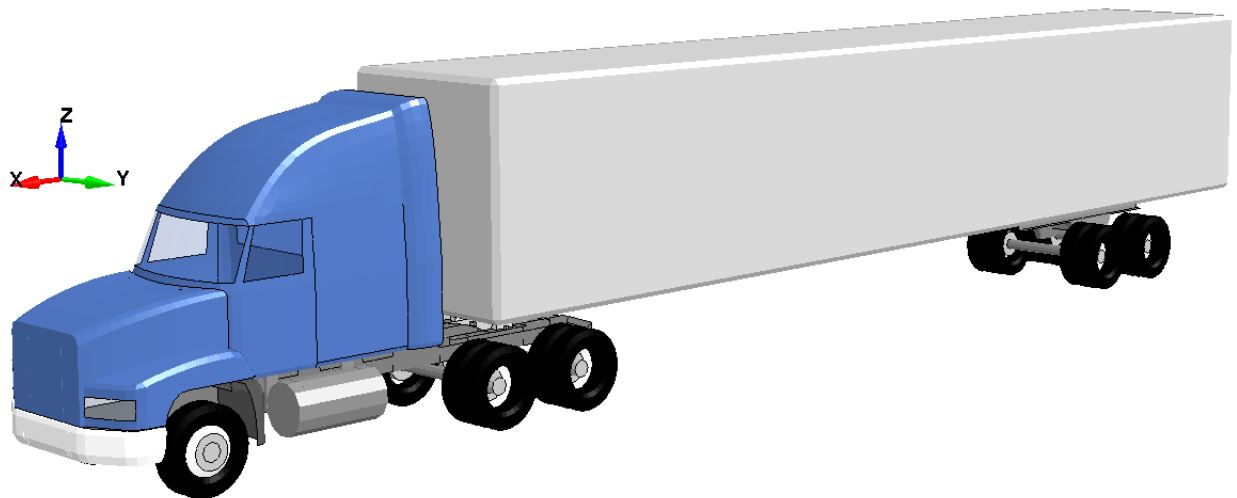


Figure 3.3.34: FE model of the tractor with trailer

A finite element model of a semitrailer truck and a rectangular MM-ALE domain containing air was developed by Cezary Bojanowski, who also performed initial shake-out runs of the model. The top of

the MM-ALE domain was flat and represented the bottom of the bridge—bridge support beam details were not included. The all-air simulations reported here were performed by Ron Kulak. The large MM-ALE domain contains 4 sub-domains (Figure 3.3.35) that could be used to represent the salt-water-air clouds described in Technical Note TRACC-TFHRC-001. For this feasibility study, all domains contain air at the same temperature and pressure. The inclusion of salt sprays—which would have a different equation of state—is deferred. The truck was modeled as a rigid body. The mesh of the air domain was made of 4 inch hexahedral elements.

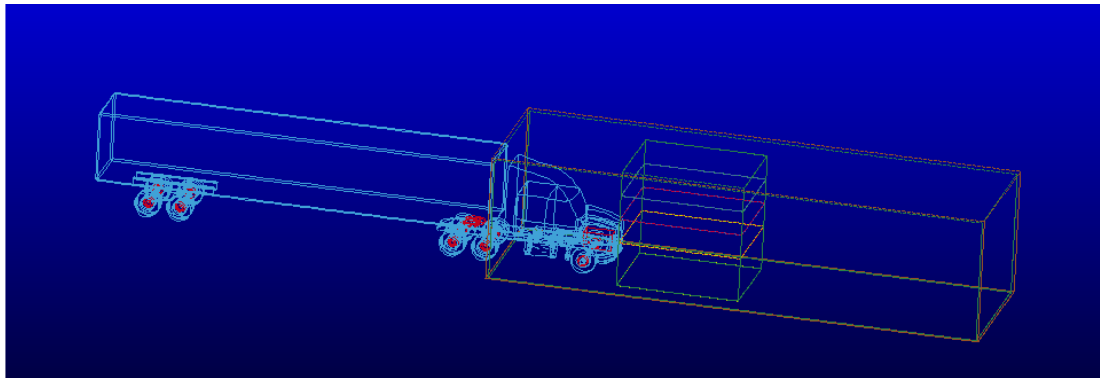
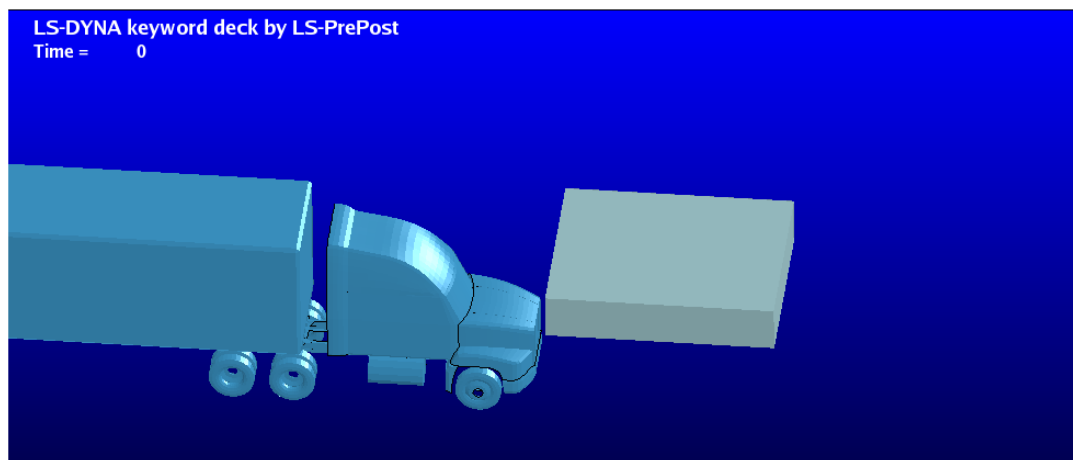


Figure 3.3.35: Semitrailer truck entering a bridge underpass

The purposes of this initial study are (1) to verify the computational characteristics estimated in Technical Note TRACC-TFHRC-001 and (2) to see if LS-DYNA gives reasonable qualitative results.

#### 3.3.5.1.3 Results

To examine the performance of the MM-ALE approach, a simulation was performed in which the semitrailer was “driven” through the bridge underpass at 60 mph and the motion of the air was qualitatively studied. The block of air second from the bottom of the bridge (Figure 3.3.36) was chosen for visualization.



(a)

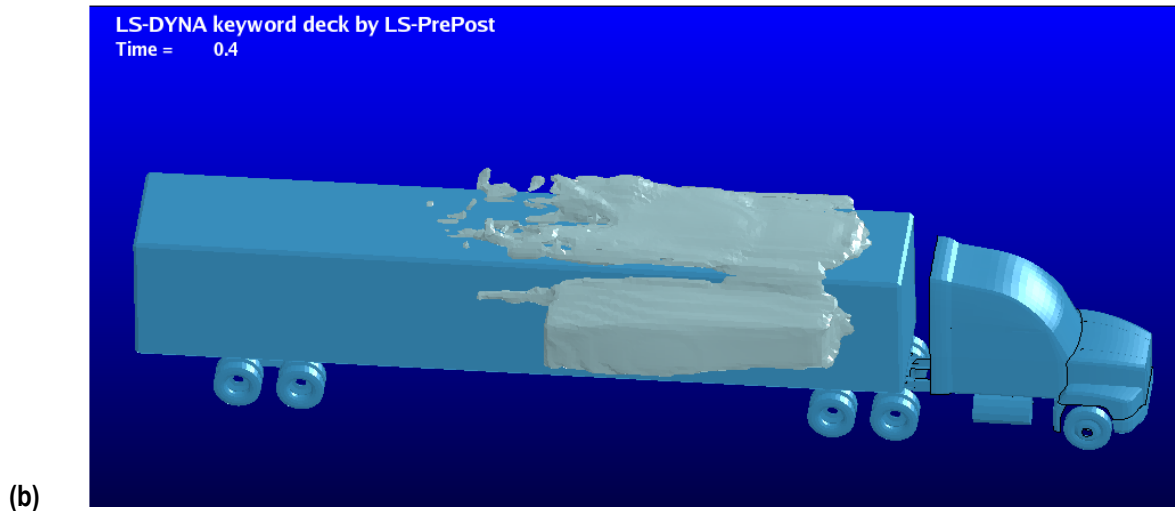


Figure 3.3.36: Semi-trailer truck impacting a layer of air in a bridge underpass:  
(a) at the beginning of the simulation; and (b) at simulation time of 0.40 seconds

From Figure 3.3.36 b, it is seen that the air behaves in a reasonable fashion as it travels past the truck and is contained by the underside of the bridge. Associated videos (separate attachment) clearly show the transient response of the air.

Table 3.8: Computational statistics

Number of nodes	12
Number of cores	96
Simulation time	0.40 sec
CPU time	1hr 0 m 33 sec
Initial time step	225e-06
Final time step	10.2e-6

The computational statistics are shown in Table 3.8. Although further studies are needed, the numbers are extremely encouraging. Using 12 nodes (96 cores), a simulation time of 0.40 seconds required only 1 hr of CPU time. It should be noted that at 60 mph, the truck would travel 35 ft during the 0.40 sec. The initial time step of 225  $\mu$ sec was reduced to 10 $\mu$ sec, which is in the ballpark of time steps used in crash analysis.

#### 3.3.5.1.4 Conclusion

A feasibility study was performed to see if the use of the multi-material Arbitrarily Lagrangian Eulerian solver in LS-DYNA/MPP could be applied to the steel weathering problem that Turner Fairbank Highway Research Center is interested in having TRACC work on. As pointed out in Technical Note TRACC-TFHRC-00, this problem has a lot of the characteristics associated with crash analysis, and, thus, it was proposed that a crash code like LS-DYNA/MPP with its new multiphysics solver MM-ALE would be a

feasible approach. The results from this study show that the use of MM-ALE is a viable approach for addressing some of the aspect of the problem. No show-stoppers were found.

#### 3.3.5.1.5 *Further study*

The successfully conducted feasibility study allowed for planning the next steps in the modeling of Salt-Spray Transport beneath Steel Bridges. TRACC is proposing to further investigate initial conditions leading to creation of salty spray clouds behind the vehicles. For this purpose detailed models of the tires and air domain surrounding it will be built (see Figure 3.3.37). Amount of water picked up and dispersed by the tire will be estimated. This will be used to estimate the location and properties of the cloud for the introduced truck - cloud interaction.

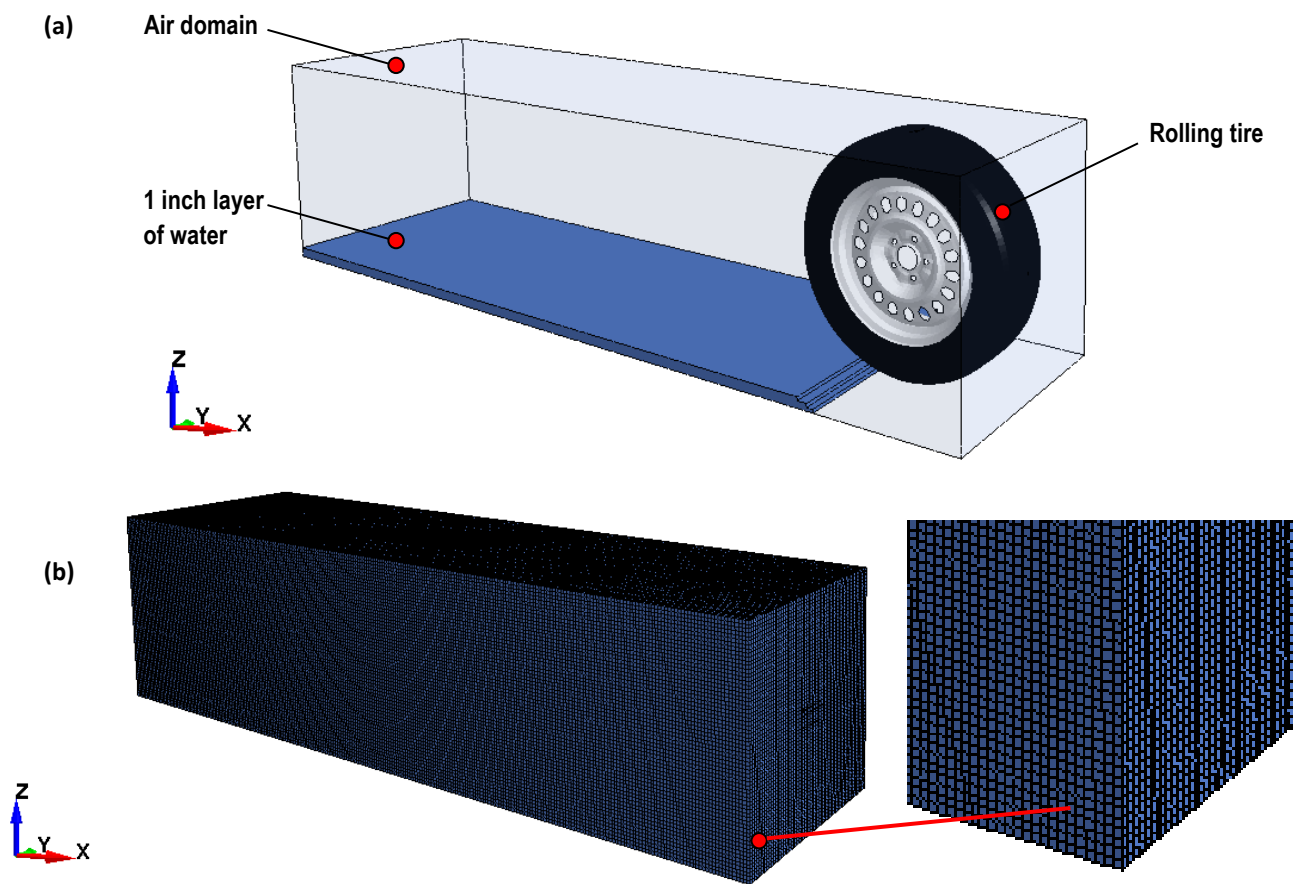


**Figure 3.3.37: Finite Element model of a Tire traveling through thin layer of water**  
 (a) Model of a tire traveling through a thin layer of water (b) computational mesh for air domain

As a further study, instead of a truck impacting into the cloud, the scenario of a car impacting into the cloud and dispersing the cloud with part of the cloud moving above the car. A truck following the car would impact the cloud (see Figure 3.3.38 —perhaps at a level above the truck’s hood—moving the cloud into the bridge’s steel beams. This simulation will represent more realistic conditions.

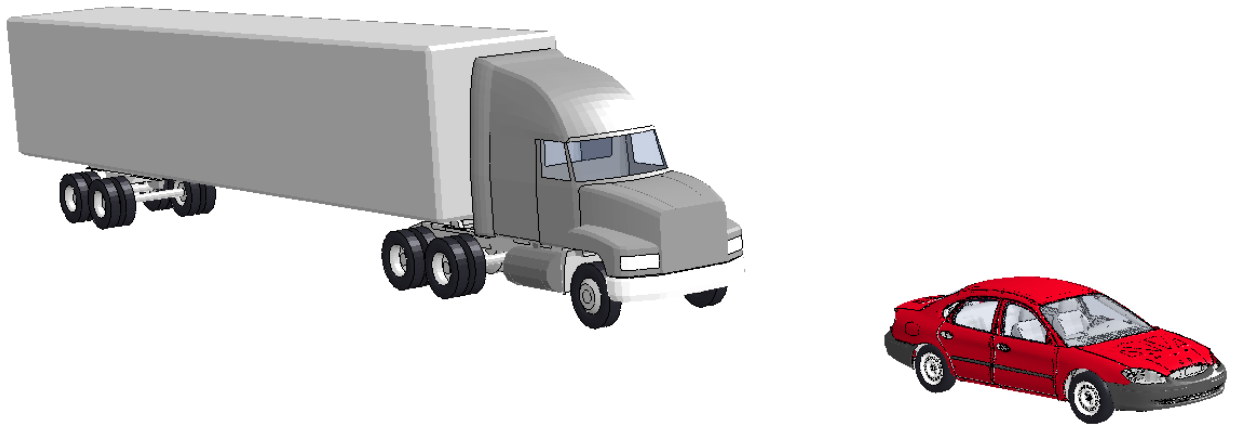


Figure 3.3.38: Finite Element model of a Tire traveling through thin layer of water